ELSEVIER

Available online at www.sciencedirect.com

SCIENCE DIRECT®

International Journal of Solids and Structures 43 (2006) 5750–5778

INTERNATIONAL JOURNAL OF SOLIDS and STRUCTURES

www.elsevier.com/locate/ijsolstr

FRP-to-concrete interfaces between two adjacent cracks: Theoretical model for debonding failure

J.G. Teng [a,*], H. Yuan [b], J.F. Chen [c]

[a] *Department of Civil and Structural Engineering, The Hong Kong Polytechnic University, Hong Kong, China*
[b] *Department of Mechanics and Civil Engineering, Jinan University, Guangzhou 510632, China*
[c] *Institute for Infrastructure and Environment, Edinburgh University, Edinburgh EH9 3JN, Scotland, UK*

Received 10 May 2005; received in revised form 4 July 2005
Available online 21 September 2005

Abstract

External bonding of fibre reinforced polymer (FRP) composites has become a popular technique for strengthening concrete structures all over the world. The performance of the interface between FRP and concrete is one of the key factors affecting the behaviour of the strengthened structure. Existing laboratory research has shown that the majority of reinforced concrete (RC) beams strengthened with a bonded FRP soffit plate fail due to debonding of the plate from the concrete. Two types of debonding failures have been commonly observed: plate end debonding and intermediate crack induced debonding. In order to understand and develop methods to predict such debonding failures, the bond behaviour between concrete and FRP has been widely studied using simple shear tests on FRP plate/sheet-to-concrete bonded joints and a great deal of research is now available on the behaviour of these bonded joints. However, for intermediate crack induced debonding failures, the debonding behaviour can be significantly different from that observed in a simple shear test. Among other factors, the most significant difference may be that the FRP plate between two adjacent cracks is subject to tension at both cracks. This paper presents an analytical solution for the debonding process in an FRP-to-concrete bonded joint model where the FRP plate is subject to tension at both ends. A realistic bi-linear local bond-slip law is employed. Expressions for the interfacial shear stress distribution and the load–displacement response are derived for different loading stages. The debonding process is discussed in detail. Finally, results from the analytical solution are presented to illustrate how the bond length affects the behaviour of such bonded joints. While the emphasis of the paper is on FRP-to-concrete joints, the analytical solution is equally applicable to similar joints between thin plates of other materials (e.g. steel and aluminium) and concrete.

Keywords: FRP; Concrete; Bond; Interface; Interfacial stress; Strengthening; Bond-slip model; Debonding

* Corresponding author. Tel.: +852 2766 6012; fax: +852 2303 1660.
E-mail address: cejgteng@polyu.edu.hk (J.G. Teng).

0020-7683/$ - see front matter © 2005 Elsevier Ltd. All rights reserved.
doi:10.1016/j.ijsolstr.2005.07.023

1. Introduction

External bonding of fibre reinforced polymer (FRP) plates or sheets (referred to as plates hereafter for simplicity) has emerged as a popular method for the strengthening or retrofitting of reinforced concrete (RC) structures (Hollaway and Leeming, 1999; Teng et al., 2002a, 2003a). In this strengthening method, the performance of the FRP-to-concrete interface in providing an effective stress transfer is of crucial importance. Indeed, a number of failure modes in FRP-strengthened RC members are directly caused by interfacial debonding between the FRP and the concrete. One of the failure modes, referred to as intermediate crack induced debonding (IC debonding), involves debonding of the FRP plate which initiates at a major crack and propagates along the FRP-to-concrete interface (Fig. 1). In RC beams flexurally strengthened with a tension face FRP plate, IC debonding may arise at a major flexural crack or flexural-shear crack (Leung, 2001; Sebastian, 2001; Teng et al., 2003b; Yao et al., 2005a). IC debonding can also arise as a result of a shear crack in RC beams shear-strengthened with FRP (Chen and Teng, 2003). In IC debonding, the interface is dominated by shear stresses, so the debonding failure is also referred to as Mode II fracture in the context of fracture mechanics.

In RC beams bonded with a tension face plate, debonding is also likely at the plate ends where debonding is due to a combination of high shear stresses and high normal stresses (Smith and Teng, 2001, 2002a,b, 2003; Shen et al., 2001; Yang et al., 2003; Pesic and Pilakoutas, 2003; Teng et al., 2002b). It should be noted that while the emphasis of the paper is on FRP-to-concrete joints, the analytical solution is equally applicable to similar joints between thin plates of other materials (e.g. steel and aluminium) and concrete. Indeed, debonding failures of RC beams bonded with steel plates have also been studied extensively in the literature (Roberts, 1989; Oehlers, 1992, 2001).

The above-mentioned IC debonding failure may be divided into two types. The first type has the feature that debonding initiates from a crack where the plate is under tension and propagates towards the free end of the plate. There is no crack between the free end of the plate and the crack where debonding initiates. This first type of debonding approximates closely IC debonding that arises from a shear crack in RC beams shear strengthened with bonded side plates, and debonding in soffit plated beams which has a single dominant flexural or flexural-shear crack. The stress state of the interface in these cases is similar to that in a simple pull test specimen in which a plate is bonded to a concrete prism and is subject to tension at one

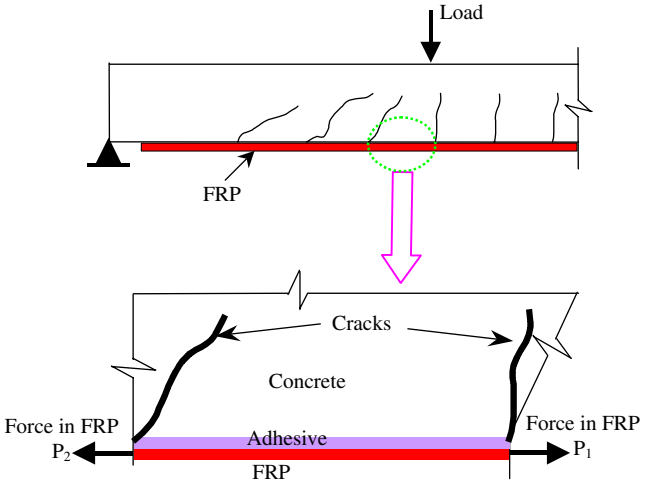

Fig. 1. Forces in an FRP plate bonded to a cracked RC beam.

end of the plate (Chen et al., 2001; Chen and Teng, 2001; Yuan et al., 2004). A large number of studies have been carried out on these simple pull tests on bonded joints and further information on this work can be found in Chen and Teng (2001), Wu et al. (2002), Teng et al. (2002a), Yuan et al. (2004). These studies suggest that the main failure mode of FRP-to-concrete joints in simple pull tests is concrete failure under shear, occurring generally in the concrete at a few millimetres from the concrete-to-adhesive interface. The ultimate load (i.e. the maximum transferable load) of the joint therefore depends strongly on concrete strength. A very important aspect of the behaviour of these bonded joints is that there exists an effective bond length beyond which an extension of the bond length cannot increase the ultimate load (Chen and Teng, 2001). Yuan et al. (2004) presented an analytical solution for the prediction of the entire debonding propagation process, which provides not only a rigorous and complete theoretical basis for understanding the full-range load–displacement behaviour of FRP-to-concrete bonded joints but also a method for identification of interfacial properties using experimental load–displacement responses. Both issues are important for the correct modelling of the FRP-to-concrete interface which is the key for the accurate prediction of the serviceability and ultimate behaviour of FRP-strengthened RC members.

In normal RC beams bonded with an FRP soffit plate, a series of cracks are generally distributed along the length of the beam. As a result, between the major flexural or flexural-shear crack where debonding initiates and the stress-free ends of the plate, other cracks exists. The mechanics of the debonding process in such beams can be significantly different from that of a simple pull test specimen as discussed above. These failures may be termed the second type of IC debonding failures to distinguish them from the first type of IC debonding failures. The behaviour of the FRP-to-concrete interface between two adjacent cracks may be idealised as the simple model shown in Fig. 2. The model resembles closely that of a simple pull test. Their chief difference lies in that both ends (i.e. at both cracks) of the FRP plate are now subject to tension in this model. Little attention has been paid to the failure of such a bonded joint model.

This paper presents an analytical solution for this simple FRP-to-concrete bonded joint (Fig. 2) to predict and better understand the behaviour of the FRP-to-concrete interface between two adjacent cracks, where the FRP plate is subjected to different tensile forces at the two ends whilst the concrete prism is subjected to two different axial forces, which may be tensile or compressive, at the two ends. A bilinear bond-slip model provides a close representation of the bond-slip behaviour of FRP-to-concrete interfaces (Yuan et al., 2004), and such a realistic bi-linear local bond-slip model is employed for the prediction of the entire debonding propagation process in the model. Numerical examples are presented to illustrate the different

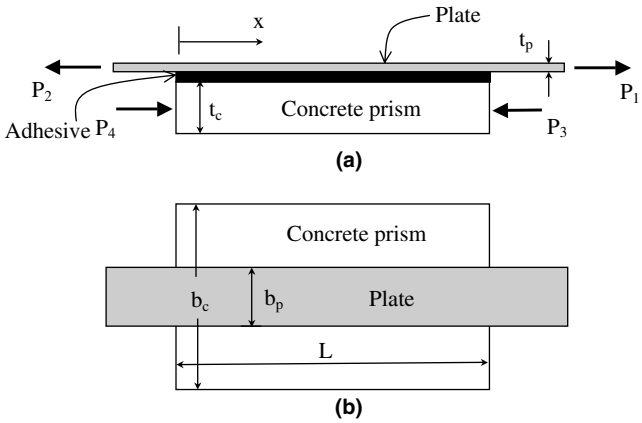

Fig. 2. Idealized model of FRP-to-concrete bonded joint between two adjacent cracks. (a) Elevation; (b) plan.

failure processes that may happen in such bonded joints. The results of this study shall provide valuable insight into the behaviour of IC debonding failures in flexurally strengthened RC structures.

It should be noted that the term "ultimate load", which is the maximum load capacity of the joint, is used in this paper instead of "bond strength" to avoid confusion with the local bond strength of the interface.

2. Governing equations

The plate in the plate-to-concrete bonded joint model as shown in Fig. 2 is subject to two tensile forces, P_1 at the right end and P_2 at the left end. Without loss of generality, it is assumed that $P_1 \geqslant P_2 \geqslant 0$. The concrete prism is assumed to be subject to two forces P_3 and P_4 which can be either compressive or tensile. Note that P_1 and P_2 are assumed to be positive when they are tensile, whilst P_3 and P_4 are assumed to be positive when they are compressive. It is also assumed that all these forces remain proportional to each other throughout the loading process. The width and thickness of the plate are denoted by b_p and t_p, respectively, and those of the concrete prism by b_c and t_c, respectively. They are assumed to be constant along the length. The bonded length of the plate (i.e. bond length) is denoted by L. The Young's modulus of the plate and concrete are E_p and E_c, respectively. The adhesive layer is assumed to have a constant thickness and the whole model is in a plane stress state.

The adhesive layer in such a model is mainly subject to shear deformations. In the present analysis, the deformation of the actual adhesive layer and those of a thin layer of adjacent concrete is lumped together and referred to as the deformation of the interface. Clearly, the failure mode of the interface is predominantly mode II interfacial fracture. A simple mechanical model for this bonded joint may thus be established by assuming that the plate and the concrete prism (the two adherends) are subject to axial deformation only while the interface is subject to pure shear deformation only. That is, all bending deformation of both adherends is neglected and the shear stress across the thickness of the adhesive layer is constant.

A horizontal coordinate system originating from the left end of the adhesive layer is adopted (Fig. 2). The left and right ends of the adhesive layer are termed the left loaded end and the right loaded end, respectively, in this paper, which are also referred to as the left end and the right end for simplicity.

Similar to simple FRP-to-concrete pull tests (Yuan et al., 2004), equilibrium considerations can lead to the following fundamental equations using the above assumptions (Fig. 3):

$$\frac{\mathrm{d}\sigma_p}{\mathrm{d}x} - \frac{\tau}{t_p} = 0 \tag{1}$$

$$\sigma_p t_p b_p + \sigma_c t_c b_c = P = P_1 - P_3 = P_2 - P_4 \tag{2}$$

where τ is the shear stress in the adhesive layer, σ_p is the axial stress in the plate and σ_c is the axial stress in the concrete prism.

The constitutive equations for the interface and the two adherends can be expressed as

$$\tau = f(\delta) \tag{3}$$

$$\sigma_p = E_p \frac{\mathrm{d}u_p}{\mathrm{d}x} \tag{4}$$

$$\sigma_c = E_c \frac{\mathrm{d}u_c}{\mathrm{d}x} \tag{5}$$

In Eq. (3), the interfacial slip δ is defined as the relative displacement between the two adherends:

$$\delta = u_p - u_c \tag{6}$$

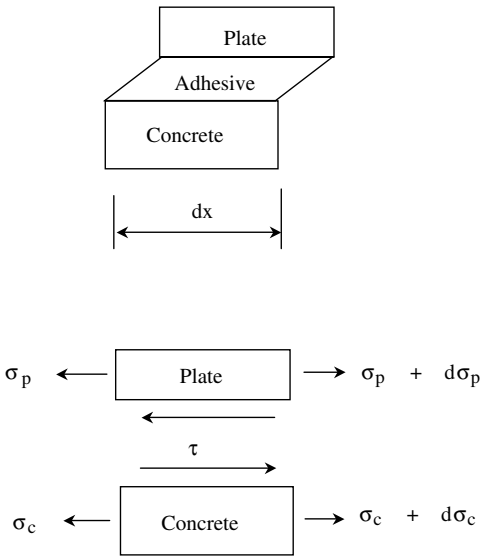

Fig. 3. Deformation and stresses.

Substituting Eqs. (2)–(6) into Eq. (1) and introducing the parameters of local bond strength τ_f and interfacial fracture energy G_f yield the following governing differential equation:

$$\frac{d^2\delta}{dx^2} - \frac{2G_f}{\tau_f^2}\lambda^2 f(\delta) = 0 \tag{7}$$

and the plate stress

$$\sigma_p = \frac{\tau_f^2}{2G_f t_p \lambda^2}\left(\frac{d\delta}{dx} + \frac{P}{b_c E_c t_c}\right) \tag{8}$$

where

$$\lambda^2 = \frac{\tau_f^2}{2G_f}\left(\frac{1}{E_p t_p} + \frac{b_p}{b_c E_c t_c}\right) \tag{9}$$

Eq. (7) may be solved if the local bond-slip model $f(\delta)$ relating the local interfacial shear stress τ to the local shear slip δ is defined. The interfacial fracture energy G_f, representing the area under the local bond-slip curve, is introduced because it may be used without knowing the exact shape of the local bond-slip curve.

3. Local bond-slip model

Various bond-slip models have been considered in previous work. Recent experimental and theoretical studies have shown that the bilinear model as shown in Fig. 4 which features a linear ascending branch followed by a linear descending branch represents a close approximation (Yuan et al., 2004). In this model, the bond shear stress increases linearly with the interfacial slip until it reaches the peak stress τ_f at which the

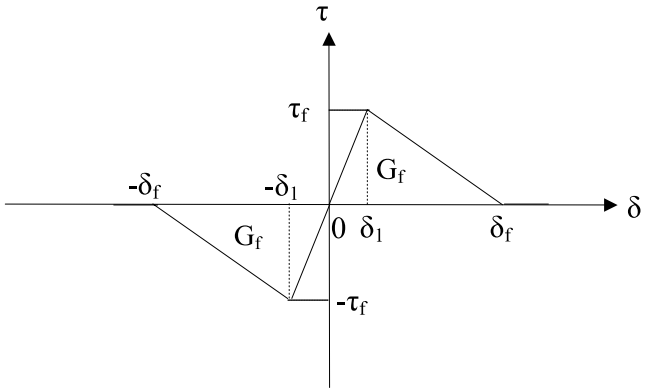

Fig. 4. Local bond-slip model.

value of the slip is denoted by δ_1. Interfacial softening (or micro-cracking) then starts with the shear stress reducing linearly with the increase of the interfacial slip. The shear stress reduces to zero when the slip equals δ_f, signifying the shear fracture (or debonding or macro-cracking) of a local bond element. The absence of any residual shear strength after debonding implies that friction and aggregate interlock in the debonded area is ignored. Considering both positive and negative slips, the bond-slip model as shown in Fig. 4 can be mathematically described by the following equation:

$$f(\delta)=\begin{cases}\dfrac{\tau_f}{\delta_1}\delta & \text{when } 0\leqslant|\delta|\leqslant\delta_1\\ \dfrac{\tau_f}{\delta_f-\delta_1}(\delta_f-\delta) & \text{when } \delta_1<\delta\leqslant\delta_f\\ \dfrac{\tau_f}{\delta_f-\delta_1}(-\delta_f-\delta) & \text{when } -\delta_f\leqslant\delta<-\delta_1\\ 0 & \text{when } |\delta|>\delta_f\end{cases} \tag{10}$$

It may be noted that before the slip reaches the ultimate value $\pm\delta_f$, the bond-slip relationship is assumed to be fully reversible when local unloading is experienced. Note that this assumption is true when the bond is still elastic but cannot be satisfied in practice if the bond has entered the softening stage. However, in the present case, local unloading after softening only occurs in a very small zone at one end of the bond length (Fig. 5e). Therefore, this assumption can significantly simplify the analysis without significant loss of accuracy.

4. Analysis of the debonding process

4.1. Loading stages up to failure

Once the bond-slip model is defined, the governing Eq. (7) can be solved to find the shear stress distribution along the interface and the load–displacement response of the bonded joint in Fig. 2. At a certain loading level, a given location of the interface may be in one of the three possible states: (1) elastic (State I); softening (State II) and debonded (State III). For convenience of reference, the interface is said to be in an elastic state (or E state) if the whole interface is elastic (Fig. 5a); in elastic–softening (E–S) state if the left part of the interface is in the elastic state whilst the right part is in the softening state (Fig. 5c); in the softening–elastic–softening (S–E–S) state if it is in softening, elastic and softening states from the left to the right, respectively (Fig. 5e), and so on.

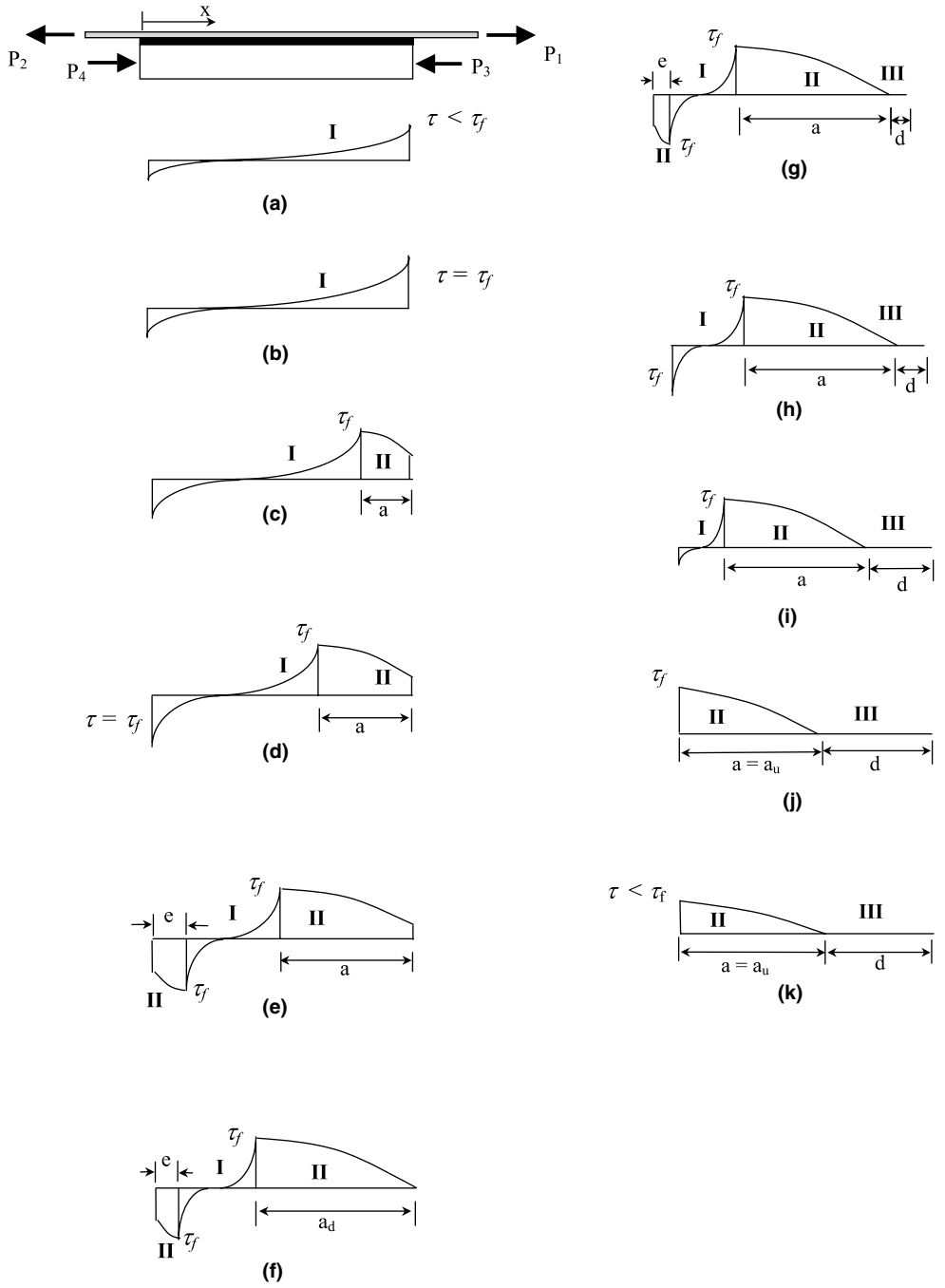

Fig. 5. Interfacial shear stress distributions at various stages (reference case). (a) Elastic stress state (OA in Fig. 7). (b) Initiation of softening at $x = L$ (point A in Fig. 7). (c) Propagation of softening zone (AB in Fig. 7). (d) Initiation of softening at $x = 0$ (point B in Fig. 7). (e) Propagation of both softening zones (BC in Fig. 7). (f) Initiation of debonding at $x = L$ (point C in Fig. 7). (g) Propagation of debonding (CD in Fig. 7). (h) Disappearance of softening at $x = 0$ (point D in Fig. 7). (i) Propagation of debonding (DE in Fig. 7). (j) Peak shear stress at $x = 0$ (point E in Fig. 7). (k) Linear unloading (EF in Fig. 7).

During the whole loading process, the interface may experience all or some of the following stages dependent on various parameters:

(a) elastic stage: the whole interface is linearly elastic ($\delta \leqslant \delta_1$) when the applied loads are small;
(b) elastic–softening stage: as the loads increase, the interface near one or both ends enters the softening state ($\delta_1 < \delta \leqslant \delta_f$) while the rest is still linearly elastic;
(c) elastic–softening–debonding stage: when the loads further increase, debonding ($\delta > \delta_f$) occurs at one end;
(d) softening–debonding stage: debonding has progressed so far that no elastic zone remains for the whole interface;
(e) softening stage: when the bond length L is very small.

The solutions for all stages are presented below. The interfacial stress distributions and debonding propagation for a typical failure process as illustrated in Fig. 5 are used here to illustrate some typical stages. Detailed debonding analysis is illustrated through numerical examples later in the paper.

4.2. Elastic stage

When the loads are small, the whole interface is in an elastic stress state (Fig. 5a). This is true as long as the interfacial shear stress $\tau \leqslant \tau_f$ (or $\delta \leqslant \delta_1$) at $x = L$. Substituting Eq. (10) for the case of $|\delta| \leqslant \delta_1$ into Eq. (7) gives the following differential equation:

$$\frac{d^2\delta}{dx^2} - \lambda_1^2\delta = 0 \tag{11}$$

where

$$\lambda_1^2 = \lambda^2 \frac{2G_f}{\delta_1\tau_f} = \frac{\tau_f}{\delta_1}\left(\frac{1}{E_p t_p} + \frac{b_p}{b_c E_c t_c}\right) \tag{12}$$

Using the following boundary conditions

$$\sigma_p = \frac{P_2}{b_p t_p} \quad \text{at } x = 0 \tag{13}$$

$$\sigma_p = \frac{P_1}{b_p t_p} \quad \text{at } x = L \tag{14}$$

the interfacial slip, interfacial shear stress and axial stress in the plate can be found by solving Eq. (11)

$$\delta = \left[\left(\frac{P_1}{b_p E_p t_p} + \frac{P_3}{b_c E_c t_c}\right)\frac{1}{\lambda_1 \sinh(\lambda_1 L)} - \left(\frac{P_2}{b_p E_p t_p} + \frac{P_4}{b_c E_c t_c}\right)\frac{1}{\lambda_1 \tanh(\lambda_1 L)}\right]\cosh(\lambda_1 x) + \left(\frac{P_2}{b_p E_p t_p} + \frac{P_4}{b_c E_c t_c}\right)\frac{1}{\lambda_1}\sinh(\lambda_1 x) \tag{15}$$

$$\tau = \frac{\tau_f}{\delta_1}\left[\left(\frac{P_1}{b_p E_p t_p} + \frac{P_3}{b_c E_c t_c}\right)\frac{1}{\lambda_1 \sinh(\lambda_1 L)} - \left(\frac{P_2}{b_p E_p t_p} + \frac{P_4}{b_c E_c t_c}\right)\frac{1}{\lambda_1 \tanh(\lambda_1 L)}\right]\cosh(\lambda x) + \frac{\tau_f}{\delta_1}\left(\frac{P_2}{b_p E_p t_p} + \frac{P_4}{b_c E_c t_c}\right)\frac{1}{\lambda_1}\sinh(\lambda_1 x) \tag{16}$$

$$\sigma_p = \left\{\left[\left(\frac{P_1}{b_p E_p t_p} + \frac{P_3}{b_c E_c t_c}\right)\frac{1}{\sinh(\lambda_1 L)} - \left(\frac{P_2}{b_p E_p t_p} + \frac{P_4}{b_c E_c t_c}\right)\frac{1}{\tanh(\lambda_1 L)}\right]\sinh(\lambda_1 x) + \left(\frac{P_2}{b_p E_p t_p} + \frac{P_4}{b_c E_c t_c}\right)\cosh(\lambda_1 x) + \frac{P}{b_c E_c t_c}\right\}\frac{\tau_f^2}{2G_f\lambda^2 t_p} \tag{17}$$

The slip at the right end (i.e. δ at $x = L$) and that at the left end (i.e. δ at $x = 0$) may be denoted by Δ_l and Δ_0, respectively. These are relative displacements between the plate and the substrate at $x = 0$ and $x = L$, are referred to as displacements in the rest of the paper. Their relationships with the loads can be obtained from Eq. (15):

$$\Delta_0 = \left(\frac{P_1}{b_p E_p t_p} + \frac{P_3}{b_c E_c t_c}\right)\frac{1}{\lambda_1 \sinh(\lambda_1 L)} - \left(\frac{P_2}{b_p E_p t_p} + \frac{P_4}{b_c E_c t_c}\right)\frac{1}{\lambda_1 \tanh(\lambda_1 L)} \tag{18}$$

$$\Delta_l = \left(\frac{P_1}{b_p E_p t_p} + \frac{P_3}{b_c E_c t_c}\right)\frac{1}{\lambda_1 \tanh(\lambda_1 L)} - \left(\frac{P_2}{b_p E_p t_p} + \frac{P_4}{b_c E_c t_c}\right)\frac{1}{\lambda_1 \sinh(\lambda_1 L)} \tag{19}$$

Let

$$P_2 = \beta P_1 \tag{20}$$

$$P_3 = \eta P_1 \tag{21}$$

P_4 and $P = P_1 - P_3$ can be expressed in terms of β ($\beta \leqslant 1$), η and P_1 from Eq. (2):

$$P_4 = (\beta + \eta - 1)P_1 \tag{22}$$

$$P = (1 - \eta)P_1 \tag{23}$$

Using Eqs. (20)–(23), Eqs. (18) and (19) can be expressed as

$$\Delta_0 = \left[\left(\frac{1}{b_p E_p t_p} + \frac{\eta}{b_c E_c t_c}\right)\frac{1}{\lambda_1 \sinh(\lambda_1 L)} - \left(\frac{\beta}{b_p E_p t_p} + \frac{\beta + \eta - 1}{b_c E_c t_c}\right)\frac{1}{\lambda_1 \tanh(\lambda_1 L)}\right]P_1 \tag{24}$$

$$\Delta_l = \left[\left(\frac{1}{b_p E_p t_p} + \frac{\eta}{b_c E_c t_c}\right)\frac{1}{\lambda_1 \tanh(\lambda_1 L)} - \left(\frac{\beta}{b_p E_p t_p} + \frac{\beta + \eta - 1}{b_c E_c t_c}\right)\frac{1}{\lambda_1 \sinh(\lambda_1 L)}\right]P_1 \tag{25}$$

It is evident that $\Delta_l \geqslant |\Delta_0|$. Therefore, with the increase of load, softening appears either firstly at $x = L$ or simultaneously at $x = 0$ and $x = L$, depending on whether $\beta < 1$ or $\beta = 1$.

4.3. Elastic–softening stage

Once the shear stress τ reaches τ_f at $x = L$ ($\Delta_l = \delta_1$) (Fig. 5b), the interface there enters the softening state (State II) while the rest remains elastic (State I) (Fig. 5c). There are three possible processes: (a) when $\beta = 1$, softening appears simultaneously at both ends; (b) when β is small, the length of the softening zone at the right increases with the load and this process continues until debonding appears at $x = L$ while the interface remains elastic at $x = 0$; (c) for other β values softening appears firstly at $x = L$ and then appears at $x = 0$ before debonding appears at $x = L$ (Fig. 5d). Therefore, the interface can be in either elastic–softening (E–S) state (Fig. 5c) or softening–elastic–softening (S–E–S) state (Fig. 5e), with (a) being a special (anti-symmetrical) S–E–S interface. Solutions for both interfaces are considered as follows.

The following governing equations for the elastic–softening stage can be obtained by substituting relevant relationships in Eq. (10) into Eq. (7):

$$\frac{d^2\delta}{dx^2} - \lambda_1^2\delta = 0 \quad \text{for } 0 \leqslant |\delta| \leqslant \delta_1 \tag{26}$$

$$\frac{d^2\delta}{dx^2} + \lambda_2^2\delta = \lambda_2^2\delta_f \quad \text{for } \delta_1 < \delta \leqslant \delta_f \tag{27}$$

$$\frac{d^2\delta}{dx^2} + \lambda_2^2\delta = -\lambda_2^2\delta_f \quad \text{for } -\delta_f < \delta \leqslant -\delta_1 \tag{28}$$

where

$$\lambda_2^2 = \lambda^2 \frac{2G_f}{(\delta_f - \delta_1)\tau_f} = \frac{\tau_f}{\delta_f - \delta_1}\left(\frac{1}{E_p t_p} + \frac{b_p}{b_c E_c t_c}\right) \tag{29}$$

4.3.1. Elastic–softening (E–S) interface

Assuming that the softening length at right is a, the elastic zone length at left equals L-a (Fig. 5c). The solutions to Eqs. (26) and (27) are of similar form to Eqs. (15)–(17) and can be derived using the following boundary conditions:

$$\sigma_p = \frac{P_2}{b_p t_p} \quad \text{at } x = 0 \tag{30}$$

$$\sigma_p \text{ is continuous} \quad \text{at } x = L - a \tag{31}$$

$$\delta = \delta_1 \text{ or } \tau = \tau_f \quad \text{at } x = L - a \tag{32}$$

$$\sigma_p = \frac{P_1}{t_p b_p} \quad \text{at } x = L \tag{33}$$

The solution for the elastic region of the interface [$0 \leqslant \delta \leqslant \delta_1$ within $0 \leqslant x \leqslant L - a$] is given by

$$\delta = \left[\frac{\delta_1}{\cosh[\lambda_1(L-a)]} - \frac{1}{\lambda_1}\left(\frac{P_2}{b_p E_p t_p} + \frac{P_4}{b_c E_c t_c}\right)\tanh(\lambda_1 L - \lambda_1 a)\right]\cosh(\lambda_1 x) + \frac{1}{\lambda_1}\left(\frac{P_2}{b_p E_p t_p} + \frac{P_4}{b_c E_c t_c}\right)\sinh(\lambda_1 x) \tag{34}$$

$$\tau = \frac{\tau_f}{\delta_1}\left[\frac{\delta_1}{\cosh[\lambda_1(L-a)]} - \frac{1}{\lambda_1}\left(\frac{P_2}{b_p E_p t_p} + \frac{P_4}{b_c E_c t_c}\right)\tanh(\lambda_1 L - \lambda_1 a)\right]\cosh(\lambda_1 x) + \frac{\tau_f}{\delta_1}\cdot\frac{1}{\lambda_1}\left(\frac{P_2}{b_p E_p t_p} + \frac{P_4}{b_c E_c t_c}\right)\sinh(\lambda_1 x) \tag{35}$$

$$\sigma_p = \frac{\tau_f^2 \lambda_1}{2G_f t_p \lambda^2}\left\{\left[\frac{\delta_1}{\cosh[\lambda_1(L-a)]} - \frac{1}{\lambda_1}\left(\frac{P_2}{b_p E_p t_p} + \frac{P_4}{b_c E_c t_c}\right)\tanh(\lambda_1 L - \lambda_1 a)\right]\sinh(\lambda_1 x) + \frac{1}{\lambda_1}\left(\frac{P_2}{b_p E_p t_p} + \frac{P_4}{b_c E_c t_c}\right)\cosh(\lambda_1 x) + \frac{P}{\lambda_1 b_c E_c t_c}\right\} \tag{36}$$

and that for the softening region of the interface [$\delta_1 < \delta \leqslant \delta_f$ within $L - a \leqslant x \leqslant L$] is given by

$$\delta = \left\{\frac{\lambda_1}{\lambda_2}\delta_1 \tanh[\lambda_1(L-a)] + \frac{1}{\lambda_2}\left(\frac{P_2}{b_p E_p t_p} + \frac{P_4}{b_c E_c t_c}\right)\frac{1}{\cosh[\lambda_1(L-a)]}\right\}\sin[\lambda_2(x - L + a)] + (\delta_1 - \delta_f)\cos[\lambda_2(x - L + a)] + \delta_f \tag{37}$$

$$\tau = -\frac{\tau_f}{\delta_f - \delta_1}\left\{\frac{\lambda_1}{\lambda_2}\delta_1 \tanh[\lambda_1(L-a)] + \frac{1}{\lambda_2}\left(\frac{P_2}{b_p E_p t_p} + \frac{P_4}{b_c E_c t_c}\right)\frac{1}{\cosh[\lambda_1(L-a)]}\right\}\sin[\lambda_2(x - L + a)] + \tau_f \cos[\lambda_2(x - L + a)] \tag{38}$$

$$\sigma_p = \frac{\tau_f^2 \lambda_2}{2G_f t_p \lambda^2}\left\{\left[\frac{\lambda_1}{\lambda_2}\delta_1 \tanh[\lambda_1(L-a)] + \frac{1}{\lambda_2}\left(\frac{P_2}{b_p E_p t_p} + \frac{P_4}{b_c E_c t_c}\right)\frac{1}{\cosh[\lambda_1(L-a)]}\right]\cos[\lambda_2(x - L + a)] - (\delta_1 - \delta_f)\sin[\lambda_2(x - L + a)] + \frac{P}{\lambda_2 b_c E_c t_c}\right\} \tag{39}$$

Substituting Eq. (33) into Eq. (39) yields

$$P_1 = \frac{\lambda_1\delta_1 \sinh[\lambda_1(L-a)]\cos(\lambda_2 a) + \lambda_2(\delta_f - \delta_1)\cosh[\lambda_1(L-a)]\sin(\lambda_2 a)}{\frac{1}{b_p E_p t_p}[\cosh(\lambda_1 L - \lambda_1 a) - \beta\cos(\lambda_2 a)] + \frac{1}{b_c E_c t_c}[\eta\cosh(\lambda_1 L - \lambda_1 a) - (\beta+\eta-1)\cos(\lambda_2 a)]} \tag{40}$$

The displacement at $x = 0$ and $x = L$ can be obtained from Eqs. (34) and (37), respectively

$$\Delta_0 = \frac{\delta_1}{\cosh[\lambda_1(L-a)]} - \frac{1}{\lambda_1}\left(\frac{\beta}{b_p E_p t_p} + \frac{\beta+\eta-1}{b_c E_c t_c}\right) P_1 \tanh(\lambda_1 L - \lambda_1 a) \tag{41}$$

$$\Delta_l = \left\{\frac{\lambda_1}{\lambda_2}\delta_1 \tanh[\lambda_1(L-a)] + \frac{1}{\lambda_2}\left(\frac{\beta}{b_p E_p t_p} + \frac{\beta+\eta-1}{b_c E_c t_c}\right) P_1 \frac{1}{\cosh[\lambda_1(L-a)]}\right\}\sin(\lambda_2 a) + (\delta_1 - \delta_f)\cos(\lambda_2 a) + \delta_f \tag{42}$$

4.3.2. Softening–elastic–softening (S–E–S) interface

Let the lengths of the softening zones at left and right equal e and a, respectively (Fig. 5e). The solutions to Eqs. (26)–(28) can be obtained by using the following boundary conditions

$$\sigma_p = \frac{P_2}{b_p t_p} \quad \text{at } x = 0 \tag{43}$$

$$\sigma_p \text{ is continuous at } x = e \quad \text{and } x = L - a \tag{44}$$

$$\delta = -\delta_1 \text{ or } \tau = -\tau_f \quad \text{at } x = e \tag{45}$$

$$\delta = \delta_1 \text{ or } \tau = \tau_f \quad \text{at } x = L - a \tag{46}$$

$$\sigma_p = \frac{P_1}{t_p b_p} \quad \text{at } x = L \tag{47}$$

The solution for the left softening region of the interface [$\delta_1 < \delta \leqslant \delta_f$ within $0 \leqslant x \leqslant e$] is given by

$$\delta = \frac{\lambda_1}{\lambda_2}\delta_1 \tanh^{-1}\left[\frac{1}{2}\lambda_1(L-a-e)\right]\sin[\lambda_2(x-e)] + (\delta_f - \delta_1)\cos[\lambda_2(x-e)] - \delta_f \tag{48}$$

$$\tau = -\tau_f \frac{\lambda_2}{\lambda_1}\tanh^{-1}\left[\frac{1}{2}\lambda_1(L-a-e)\right]\sin[\lambda_2(x-e)] - \tau_f\cos[\lambda_2(x-e)] \tag{49}$$

$$\sigma_p = \frac{\tau_f^2}{2G_f t_p \lambda^2}\left\{\lambda_1\delta_1 \tanh^{-1}\left[\frac{1}{2}\lambda_1(L-a-e)\right]\cos[\lambda_2(x-e)] - \lambda_2(\delta_f - \delta_1)\sin[\lambda_2(x-e)] + \frac{P}{b_c E_c t_c}\right\} \tag{50}$$

The solution for the elastic region of the interface [$0 \leqslant \delta \leqslant \delta_1$ within $e \leqslant x \leqslant L - a$] is given by

$$\delta = -\delta_1\cosh[\lambda_1(x-e)] + \delta_1 \tanh^{-1}\left[\frac{1}{2}\lambda_1(L-a-e)\right]\sinh[\lambda_1(x-e)] \tag{51}$$

$$\tau = -\tau_f\cosh[\lambda_1(x-e)] + \tau_f \tanh^{-1}\left[\frac{1}{2}\lambda_1(L-a-e)\right]\sinh[\lambda_1(x-e)] \tag{52}$$

$$\sigma_p = \frac{\tau_f^2}{2G_f t_p \lambda^2}\left[-\delta_1\lambda_1\sinh[\lambda_1(x-e)] + \delta_1\lambda_1 \tanh^{-1}\left[\frac{1}{2}\lambda_1(L-a-e)\right]\cosh[\lambda_1(x-e)] + \frac{P}{b_c E_c t_c}\right] \tag{53}$$

and that for the right softening region of the interface [$\delta_1 < \delta \leqslant \delta_f$ within $L - a \leqslant x \leqslant L$] is given by

$$\delta = \frac{\lambda_1}{\lambda_2}\delta_1 \tanh^{-1}\left[\frac{1}{2}\lambda_1(L-a-e)\right]\sin[\lambda_2(x-L+a)] + (\delta_1-\delta_f)\cos[\lambda_2(x-L+a)] + \delta_f \tag{54}$$

$$\tau = -\tau_f\frac{\lambda_2}{\lambda_1}\tanh^{-1}\left[\frac{1}{2}\lambda_1(L-a-e)\right]\sin[\lambda_2(x-L+a)] + \tau_f\cos[\lambda_2(x-L+a)] \tag{55}$$

$$\sigma_p = \frac{\tau_f^2}{2G_f t_p \lambda^2}\left\{\lambda_1\delta_1\tanh^{-1}\left[\frac{1}{2}\lambda_1(L-a-e)\right]\cos[\lambda_2(x-L+a)] + (\delta_f-\delta_1)\lambda_2\sin[\lambda_2(x-L+a)] + \frac{P}{b_c E_c t_c}\right\} \tag{56}$$

Substituting Eq. (43) into Eq. (50) and Eq. (47) into Eq. (56) yields two simultaneous equations relating load P_1 to softening zone lengths e and a

$$P_1 = \lambda_2\left[\frac{\beta}{b_p E_p t_p} + \frac{\beta+\eta-1}{b_c E_c t_c}\right]^{-1} \times \left\{\frac{\lambda_1}{\lambda_2}\delta_1\tanh^{-1}\left[\frac{1}{2}\lambda_1(L-a-e)\right]\cos(\lambda_2 e) + (\delta_f-\delta_1)\sin(\lambda_2 e)\right\} \tag{57}$$

$$P_1 = \lambda_2\left[\frac{1}{b_p E_p t_p} + \frac{\eta}{b_c E_c t_c}\right]^{-1} \times \left\{\frac{\lambda_1}{\lambda_2}\delta_1\tanh^{-1}\left[\frac{1}{2}\lambda_1(L-a-e)\right]\cos(\lambda_2 a) + (\delta_f-\delta_1)\sin(\lambda_2 a)\right\} \tag{58}$$

The displacements at $x = 0$ and $x = L$ can be obtained from Eqs. (48) and (54):

$$\Delta_0 = -\frac{\lambda_1}{\lambda_2}\delta_1\tanh^{-1}\left[\frac{1}{2}\lambda_1(L-a-e)\right]\sin(\lambda_2 e) + (\delta_f-\delta_1)\cos(\lambda_2 e) - \delta_f \tag{59}$$

$$\Delta_l = \frac{\lambda_1}{\lambda_2}\delta_1\tanh^{-1}\left[\frac{1}{2}\lambda_1(L-a-e)\right]\sin(\lambda_2 a) + (\delta_1-\delta_f)\cos(\lambda_2 a) + \delta_f \tag{60}$$

If $\beta = 1$, comparing Eq. (57) with Eqs. (58) and (59) with Eq. (60) gives that $e = a$ and $\Delta_l = \Delta_0$.

4.4. Elastic–softening–debonding stage

The three types of interface considered in the previous section, including the elastic–softening–debonding (E–S–D) interface (β is small), the softening–elastic–softening–debonding (S–E–S–D) interface (β is not small) and the debonding-softening–elastic–softening–debonding (D–S–E–S–D) interface (β =1), are also considered here.

4.4.1. Elastic–softening–debonding (E–S–D) interface

This interface can be developed from the E–S interface above. Its stress distribution has the form shown in Fig. 5h. Debonding initiates when $\Delta_l = \delta_f$. Solving the following equations obtained from Eqs. (40) and (42) gives the length of the softening interface a, denoted by a_d, at the initiation of debonding:

$$P_1 = \frac{\lambda_1\delta_1\sinh[\lambda_1(L-a_d)]\cos(\lambda_2 a_d) + \lambda_2(\delta_f-\delta_1)\cosh[\lambda_1(L-a_d)]\sin(\lambda_2 a_d)}{\frac{1}{b_p E_p t_p}[\cosh(\lambda_1 L - \lambda_1 a_d) - \beta\cos(\lambda_2 a_d)] + \frac{1}{b_c E_c t_c}[\eta\cosh(\lambda_1 L - \lambda_1 a_d) - (\beta+\eta-1)\cos(\lambda_2 a_d)]} \tag{61}$$

$$P_1 = \frac{\lambda_2(\delta_f-\delta_1)\cos(\lambda_2 a_d)\cosh[\lambda_1(L-a_d)] - \lambda_1\delta_1\sin(\lambda_2 a_d)\sinh[\lambda_1(L-a_d)]}{\left(\frac{\beta}{b_p E_p t_p} + \frac{\beta+\eta-1}{b_c E_c t_c}\right)\sin(\lambda_2 a_d)} \tag{62}$$

As debonding propagates, the length of the intact interface reduces and the peak shear stress τ_f moves towards the left. A given location along the interface can be elastic (State I), softening (State II) or

debonded (i.e. stress-free) (State III). Assuming that the debonded length of the interface starting at $x = L$ is d, Eqs. (34)–(39) are still valid for the E–S–D interface here if L is replaced by $(L - d)$. Similarly, Eqs. (61) and (62) remain valid during the debonding process if L is replaced by $(L - d)$ and a_d is replaced by a.

The displacement at $x = L$ during the debonding process can be obtained from

$$\Delta_l = \delta_f + \left(\frac{1}{b_p E_p t_p} + \frac{\eta}{b_c E_c t_c}\right) P_1 d \tag{63}$$

As debonding propagates further, the peak shear stress τ_f moves continuously towards the left. The stage is completed when the peak shear stress τ_f moves to $x = 0$ so that the elastic zone disappears. The length of the softening interface at this stage, $a_u = L - d$, is termed the characteristic softening length here, and can be obtained as

$$a_u = \frac{1}{\lambda_2} \arccos\left(\frac{\frac{\beta}{b_p E_p t_p} + \frac{\beta+\eta-1}{b_c E_c t_c}}{\frac{1}{b_p E_p t_p} + \frac{\eta}{b_c E_c t_c}}\right) \tag{64}$$

4.4.2. Softening–elastic–softening–debonding (S–E–S–D) interface

For a S–E–S interface, it becomes a S–E–S–D interface (Fig. 5g) when debonding initiates at $x = L$ ($\Delta_l = \delta_f$) (Fig. 5f). The corresponding softening length a, denoted by a_d, can be found from the following equations which are obtained from Eqs. (57), (58) and (60)

$$P_1 = \lambda_2(\delta_f - \delta_1)\left[\frac{\beta}{b_p E_p t_p} + \frac{\beta + \eta - 1}{b_c E_c t_c}\right]^{-1} \frac{\cos[\lambda_2(a_d - e)]}{\sin(\lambda_2 a_d)} \tag{65}$$

$$P_1 = \lambda_2(\delta_f - \delta_1)\left[\frac{1}{b_p E_p t_p} + \frac{\eta}{b_c E_c t_c}\right]^{-1} \frac{1}{\sin(\lambda_2 a_d)} \tag{66}$$

$$\tan(\lambda_2 a_d) = \frac{\lambda_1}{\lambda_2} \tanh\left[\frac{1}{2}\lambda_1(L - a_d - e)\right] \tag{67}$$

As debonding propagates, the peak shear stress τ_f near the right end moves towards the left. Under the assumption that the whole local bond-slip relationship before debonding is fully reversible during unloading, the peak shear stress τ_f near the left end also moves towards the left to $x = 0$ and the left softening zone experiences unloading whilst the actual applied load increases. Let the debonded length of the interface at the right end equal d, Eqs. (48)–(56) remain valid if L is replaced by $(L - d)$. The load–displacement relationship can still be expressed as Eq. (63). As the interfacial shear stress is zero for $x \geqslant L - d$, the three equations relating P_1 to a, e and d can be obtained from Eqs. (65)–(67) if L is replaced by $(L-d)$ and a_d is replaced by a. From Eqs. (65) and (66), the relationship between a and e for the S–E–S–D interface can be obtained as

$$e = a - a_u \tag{68}$$

The S–E–S–D interface reduces to an E–S–D interface (Fig. 5i) after the softening length at the left e reduces to 0 (Fig. 5h). Substituting $e = 0$ into the three equations relating P_1 to a, e and d yields P_1, a and d when E–S–D interface begins, which can be analysed as in the preceding section.

4.4.3. Debonding–softening–elastic–softening–debonding (D–S–E–S–D) interface

When $\beta = 1$, debonding can start from both ends simultaneously and propagate towards the middle of the interface. At the initiation of debonding $\Delta_l - \Delta_0 = \delta_f$. The corresponding value of $a = e$, denoted by a_d, can be obtained from the following equations which are derived from Eqs. (58) and (60)

$$P_1 = \lambda_2(\delta_f - \delta_1)\left[\frac{1}{b_p E_p t_p} + \frac{\eta}{b_c E_c t_c}\right]^{-1} \frac{1}{\sin(\lambda_2 a_d)} \tag{69}$$

$$\tan(\lambda_2 a_d) = \frac{\lambda_1}{\lambda_2}\tanh\left[\frac{1}{2}\lambda_1(L - 2a_d)\right] \tag{70}$$

As debonding propagates, the peak shear stress τ_f at left and right moves towards the middle of the interface ($x = L/2$). Assuming that the debonded length of the interface at both ends is d, Eqs. (48)–(56) are valid if L is replaced by $(L - 2d)$. Therefore, the load–displacement relationship can still be expressed as Eq. (63). As the interfacial shear stress at $x = d$ and $x = L - d$ is zero, the two equations relating P_1 to a and d can be obtained from Eqs. (69) and (70) if L is replaced by $(L - 2d)$ and a_d is replaced by a.

4.5. Softening–debonding stage

The softening–debonding stage (Fig. 5k) is governed by Eq. (27) with the following boundary conditions

$$\sigma_p = \frac{P_2}{b_p t_p} \quad \text{at } x = 0 \tag{71}$$

$$\delta = \delta_f \text{ and } \sigma_p = \frac{P_1}{t_p b_p} \quad \text{at } x = a = L - d \tag{72}$$

The solution for the softening region of the interface [$\delta_1 < \delta \leqslant \delta_f$ within $0 \leqslant x \leqslant a_u$] can be found as

$$a = a_u = \frac{1}{\lambda_2}\arccos\left(\frac{\frac{\beta}{b_p E_p t_p} + \frac{\beta+\eta-1}{b_c E_c t_c}}{\frac{1}{b_p E_p t_p} + \frac{\eta}{b_c E_c t_c}}\right) \tag{73}$$

$$\delta = \delta_f - \frac{1}{\lambda_2}\left(\frac{1}{b_p E_p t_p} + \frac{\eta}{b_c E_c t_c}\right)P_1 \sin(\lambda_2 a_u - \lambda_2 x) \tag{74}$$

$$\tau = \frac{\tau_f}{\lambda_2(\delta_f - \delta_1)}\left(\frac{1}{b_p E_p t_p} + \frac{\eta}{b_c E_c t_c}\right)P_1 \sin(\lambda_2 a_u - \lambda_2 x) \tag{75}$$

$$\sigma_p = \frac{\tau_f^2}{2G_f t_p \lambda^2}\left[\left(\frac{1}{b_p E_p t_p} + \frac{\eta}{b_c E_c t_c}\right)\cos(\lambda_2 a_u - \lambda_2 x) + \frac{1-\eta}{b_c E_c t_c}\right]P_1 \tag{76}$$

Eq. (73) shows that the length of the softening zone remains constant during the softening–debonding stage. During this stage, the maximum interfacial shear stress τ at $x = 0$ reduces linearly with the load. The displacement at the right end can be obtained from

$$\Delta_l = \delta_f + \left(\frac{1}{b_p E_p t_p} + \frac{\eta}{b_c E_c t_c}\right)P_1(L - a_u) \tag{77}$$

Eq. (77) indicates that the displacement reduces linearly with the load.

4.6. Softening stage

If the bond length is so short that $L < a_u$, the interface will experience elastic, elastic–softening, softening, and linear unloading stages. The softening–debonding stage does not happen during the failure process. At the softening stage, the whole interface is in a softening state and is governed by Eq. (27) with the following boundary conditions:

$$\sigma_{\mathrm{p}} = \frac{P_2}{b_{\mathrm{p}} t_{\mathrm{p}}} \quad \text{at } x = 0 \tag{78}$$

$$\sigma_{\mathrm{p}} = \frac{P_1}{t_{\mathrm{p}} b_{\mathrm{p}}} \quad \text{at } x = L \tag{79}$$

The following solution for this stage [$\delta_1 < \delta \leqslant \delta_{\mathrm{f}}$ within $0 \leqslant x \leqslant L$] can thus be found

$$\begin{aligned}\delta = {} & \delta_{\mathrm{f}} + \frac{1}{\lambda_2}\left(\frac{\beta}{b_{\mathrm{p}} E_{\mathrm{p}} t_{\mathrm{p}}} + \frac{\beta+\eta-1}{b_{\mathrm{c}} E_{\mathrm{c}} t_{\mathrm{c}}}\right) P_1 \sin(\lambda_2 x) \\ & + \frac{1}{\lambda_2}\left[\left(\frac{\beta}{b_{\mathrm{p}} E_{\mathrm{p}} t_{\mathrm{p}}} + \frac{\beta+\eta-1}{b_{\mathrm{c}} E_{\mathrm{c}} t_{\mathrm{c}}}\right)\frac{1}{\tan(\lambda_2 L)} - \left(\frac{1}{b_{\mathrm{p}} E_{\mathrm{p}} t_{\mathrm{p}}} + \frac{\eta}{b_{\mathrm{c}} E_{\mathrm{c}} t_{\mathrm{c}}}\right)\frac{1}{\sin(\lambda_2 L)}\right] P_1 \cos(\lambda_2 x)\end{aligned} \tag{80}$$

$$\begin{aligned}\tau = {} & -\frac{\tau_{\mathrm{f}}}{\delta_{\mathrm{f}} - \delta_1}\left\{\frac{1}{\lambda_2}\left(\frac{\beta}{b_{\mathrm{p}} E_{\mathrm{p}} t_{\mathrm{p}}} + \frac{\beta+\eta-1}{b_{\mathrm{c}} E_{\mathrm{c}} t_{\mathrm{c}}}\right) P_1 \sin(\lambda_2 x)\right. \\ & \left. + \frac{1}{\lambda_2}\left[\left(\frac{\beta}{b_{\mathrm{p}} E_{\mathrm{p}} t_{\mathrm{p}}} + \frac{\beta+\eta-1}{b_{\mathrm{c}} E_{\mathrm{c}} t_{\mathrm{c}}}\right)\frac{1}{\tan(\lambda_2 L)} - \left(\frac{1}{b_{\mathrm{p}} E_{\mathrm{p}} t_{\mathrm{p}}} + \frac{\eta}{b_{\mathrm{c}} E_{\mathrm{c}} t_{\mathrm{c}}}\right)\frac{1}{\sin(\lambda_2 L)}\right] P_1 \cos(\lambda_2 x)\right\}\end{aligned} \tag{81}$$

$$\begin{aligned}\sigma_{\mathrm{p}} = {} & \frac{\tau_{\mathrm{f}}^2}{2 G_{\mathrm{f}} t_{\mathrm{p}} \lambda^2}\left\{\left(\frac{\beta}{b_{\mathrm{p}} E_{\mathrm{p}} t_{\mathrm{p}}} + \frac{\beta+\eta-1}{b_{\mathrm{c}} E_{\mathrm{c}} t_{\mathrm{c}}}\right)\cos(\lambda_2 x)\right. \\ & \left. - \left[\left(\frac{\beta}{b_{\mathrm{p}} E_{\mathrm{p}} t_{\mathrm{p}}} + \frac{\beta+\eta-1}{b_{\mathrm{c}} E_{\mathrm{c}} t_{\mathrm{c}}}\right)\frac{1}{\tan(\lambda_2 L)} - \left(\frac{1}{b_{\mathrm{p}} E_{\mathrm{p}} t_{\mathrm{p}}} + \frac{\eta}{b_{\mathrm{c}} E_{\mathrm{c}} t_{\mathrm{c}}}\right)\frac{1}{\sin(\lambda_2 L)}\right]\sin(\lambda_2 x) + \frac{1-\eta}{b_{\mathrm{c}} E_{\mathrm{c}} t_{\mathrm{c}}}\right\} P_1\end{aligned} \tag{82}$$

During this stage, the maximum interfacial shear stress at $x = 0$ reduces with the load. The displacement Δ_0 at the left loaded end can be obtained from Eq. (80) by setting $x = 0$. The load at the beginning of this stage can be found by setting $\Delta_0 = \delta_1$ in Eq. (80)

$$P_1 = \frac{(\delta_{\mathrm{f}} - \delta_1)\lambda_2 \sin(\lambda_2 L)}{\left(\frac{1}{b_{\mathrm{p}} E_{\mathrm{p}} t_{\mathrm{p}}} + \frac{\eta}{b_{\mathrm{c}} E_{\mathrm{c}} t_{\mathrm{c}}}\right)[1 - \cos(\lambda_2 a_{\mathrm{u}})\cos(\lambda_2 L)]} \tag{83}$$

The displacement Δ_l at the right loaded end ($x = L$) can also be obtained from Eq. (80)

$$\Delta_l = \delta_{\mathrm{f}} - \left(\frac{1}{b_{\mathrm{p}} E_{\mathrm{p}} t_{\mathrm{p}}} + \frac{\eta}{b_{\mathrm{c}} E_{\mathrm{c}} t_{\mathrm{c}}}\right)\left[1 - \frac{\cos(\lambda_2 a_{\mathrm{u}})}{\cos(\lambda_2 L)}\right]\frac{P_1}{\lambda_2 \tan(\lambda_2 L)} \tag{84}$$

Eq. (84) indicates that the displacement at the right end increases linearly with the reduction of the load.

5. Full-range load–displacement analysis

Fig. 6 shows the analysis flowchart for the FRP-to-concrete bonded joint model considered, where five different failure processes are identified. Depending on the geometrical, material and loading parameters, the left end of the model may or may not enter softening and debonding. For a joint model with a given set of parameters, the analysis starts with an elastic interface, and then follows different routes according to the criteria indicated in Fig. 6. Appropriate solutions for different interfaces at various stages presented above shall be used here. Detailed stress distributions along the interface at various stages and the whole load–displacement curve can be obtained from this process.

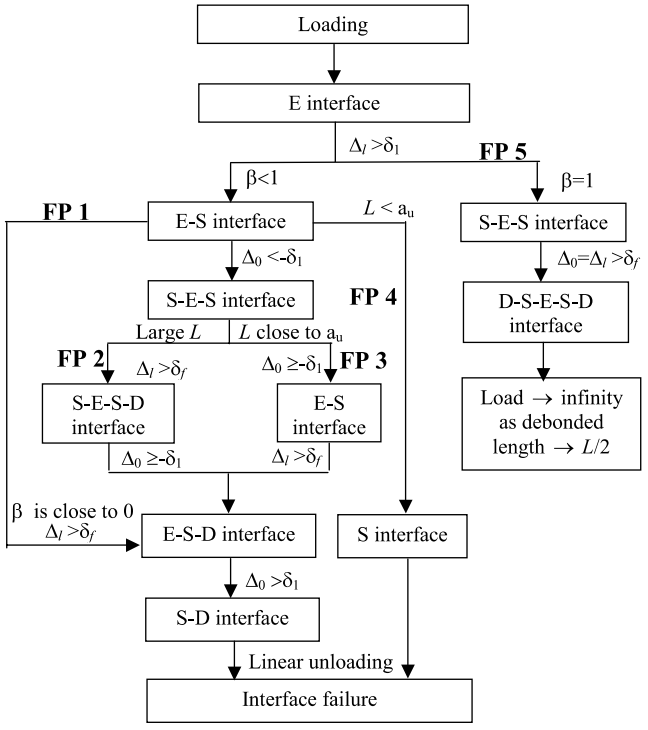

Fig. 6. Failure processes (FP).

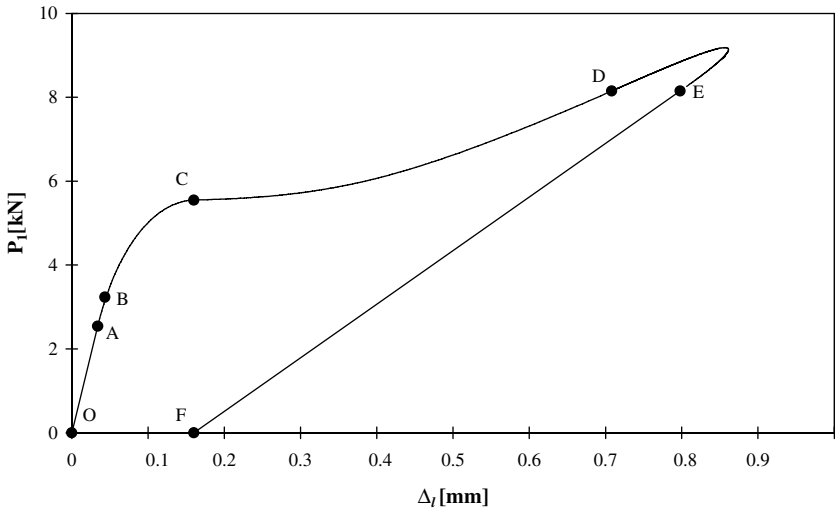

Fig. 7. Full-range load–displacement curve (reference case).

6. Failure processes and numerical examples

The five failure processes identified above are analysed here. Four numerical examples are also presented to illustrate failure processes 2–5 (Fig. 6) and their corresponding load–displacement responses of the plate-to-concrete bonded joint model. The effects of the load parameter β and the bond length on the ultimate load are also discussed. The following reference parameters, which were used in a series of simple pull tests of FRP-to-concrete bonded joints by Yao et al. (2005b), are used in all the examples unless otherwise stated: $t_p = 0.165$ mm, $b_p = 25$ mm, $t_c = 150$ mm, $b_c = 150$ mm, $E_p = 256$ GPa, $E_c = 28.6$ GPa and $f'_{cu} = 29$ MPa. The local bond-slip parameters for a typical specimen were deduced from the experimental

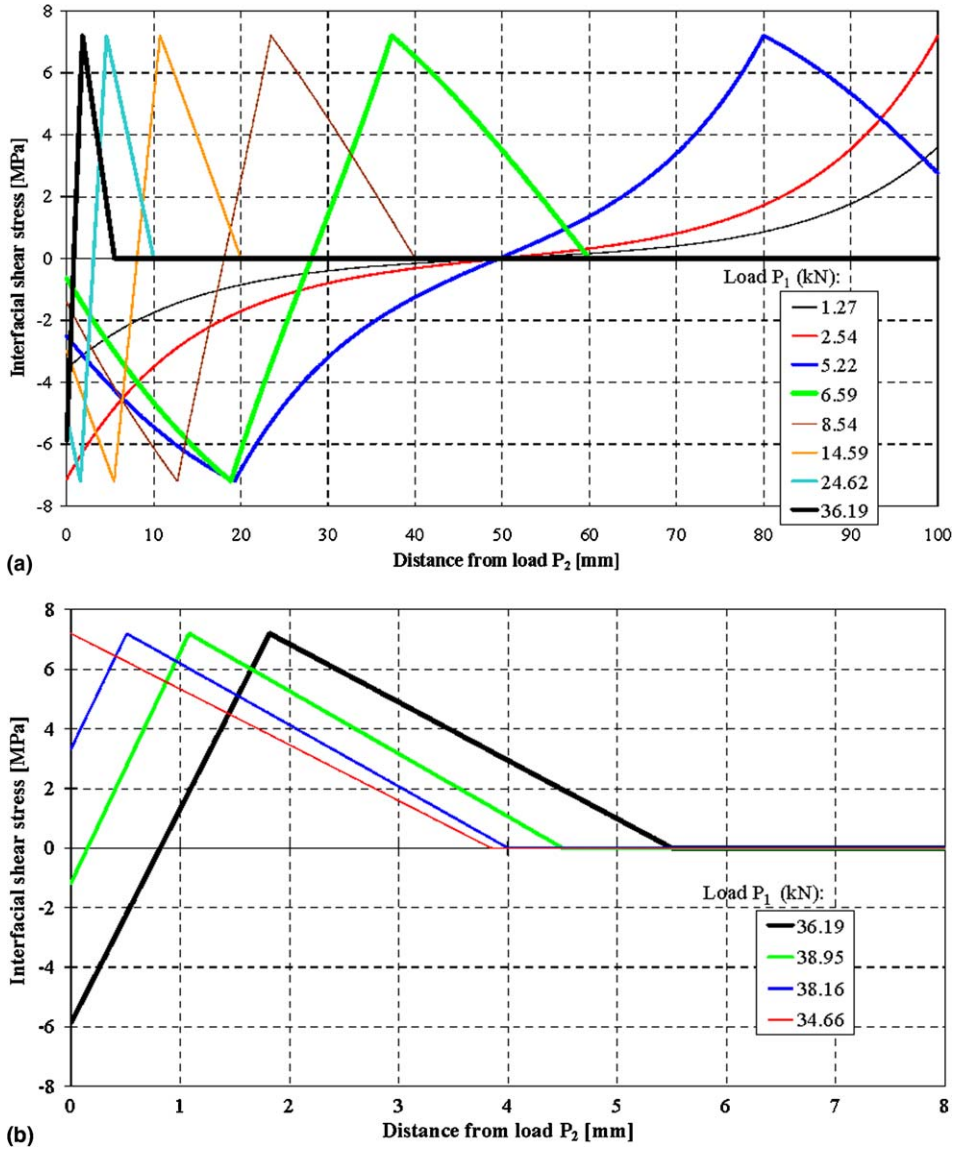

Fig. 8. Interfacial stress distributions at various stages ($\beta = 0.99$). (a) Early stages and (b) final stages.

load–displacement curve as Yuan et al. (2004): $\delta_f = 0.16$ mm, $\delta_1 = 0.034$ mm, $\tau_f = 7.2$ MPa and $G_f = 0.58$ N/mm. Unless otherwise stated, $\beta = 0.8$ and $\eta = 1$ are used. A bond length of $L = 100$ mm, which represents a typical crack spacing in reinforced concrete beams (Piyasena et al., 2004), is used unless otherwise indicated. From Eq. (64), the characteristic softening length $a_u = 17.48$ mm for these parameters.

6.1. Failure process 1 (small β and $L > a_u$)

Failure process 1 in Fig. 6 (small β and $L > a_u$) is similar to that of a simple pull test of FRP-to-concrete bonded joints with a load applied at the right end only ($\beta = 0$), in which softening does not happen at the

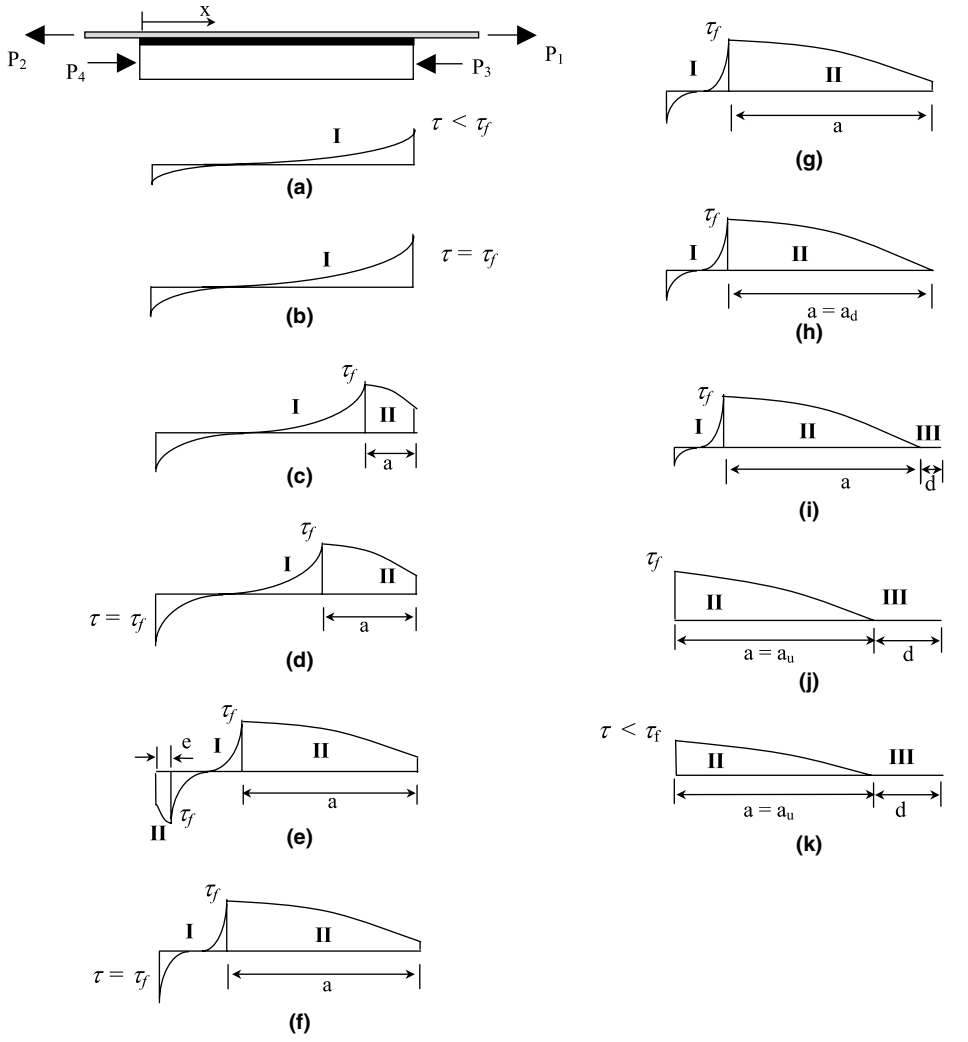

Fig. 9. Interfacial shear stress distributions at various stages ($L = 25$ mm). (a) Elastic stress state (OA in Fig. 10). (b) Initiation of softening at $x = L$ (point A in Fig. 10). (c) Propagation of softening zone (AB in Fig. 10). (d) Initiation of softening at $x = 0$ (point B in Fig. 10). (e) Propagation of both softening zones (BC in Fig. 10). (f) Disappearance of softening at $x = 0$ (point C in Fig. 10). (g) Propagation of softening zone (CD in Fig. 10). (h) Initiation of debonding at $x = L$ (point D in Fig. 10). (i) Propagation of debonding (DE in Fig. 10). (j) Peak shear stress at $x = 0$ (point E in Fig. 10). (k) Linear unloading (EF in Fig. 10).

left end (Yuan et al., 2004). When loaded to failure, the interface experiences the elastic, elastic–softening, elastic–softening–debonding, softening–debonding, and linear unloading states sequentially. More details can be found in Yuan et al. (2004).

6.2. Failure process 2 ($0 \ll \beta < 1$ and $L \gg a_u$)

Fig. 5 shows the interfacial shear stress distributions and propagation of debonding for the reference case described above with $L = 100$ mm and $\beta = 0.8$. The corresponding full-range load–displacement curve is shown in Fig. 7. When the loads are small, the entire interface is in an elastic state (Fig. 5a and OA in Fig. 7). This remains valid as long as τ at the right end ($x = L$) is smaller than τ_f. Eq. (25) indicates that the load–displacement relationship is linear at this elastic stage. Softening initiates at the right end once τ reaches τ_f at $x = L$ (Fig. 5b and point A in Fig. 7). As load P_1 increases (all other loads increase proportionally), the peak shear stress τ_f moves towards the left and the softening zone length a increases. The interface is in an elastic–softening state (Fig. 5c and AB in Fig. 7). The magnitude of the interfacial shear stress at $x = 0$ increases gradually. Softening initiates at $x = 0$ when τ attains $-\tau_f$ there (Fig. 5d and point B in Fig. 7). As load P_1 and the length of softening zone a continue to increase, the length of the softening zone e at the left also increases (Fig. 5e and BC in Fig. 7). As P_1 and a further increase, the value of e will reach its maximum value after which unloading happens in the softening zone at the left and e decreases. The unloading in the left softening zone can happen either before or after debonding at the right end starts, depending on many factors such as the geometry of the bonded joint, the FRP and concrete material properties and the load ratio P_2/P_1.

Debonding initiates at the right end when the interfacial shear stress there decreases to 0 (Fig. 5f and point C in Fig. 7) and debonding propagates towards the left thereafter. The interface is now in the softening–elastic–softening–debonding state. The left peak shear stress τ_f moves towards $x = 0$, and e reduces gradually whilst P_1 continues to increase (Fig. 5g and CD in Fig. 7). After e reduces to 0 (left peak shear stress τ_f moves back to $x = 0$ (Fig. 5h and point D in Fig. 7)), the interface enters an elastic–softening–debonding state (Fig. 5i and DE in Fig. 7). The ultimate load P_1 is attained at this stage. It may be noted that P_1 equals P_2 plus the summation of shear stresses along the interface so the maximum value of P_1 does not necessarily correspond to the maximum area of the shear stress distribution diagram. The

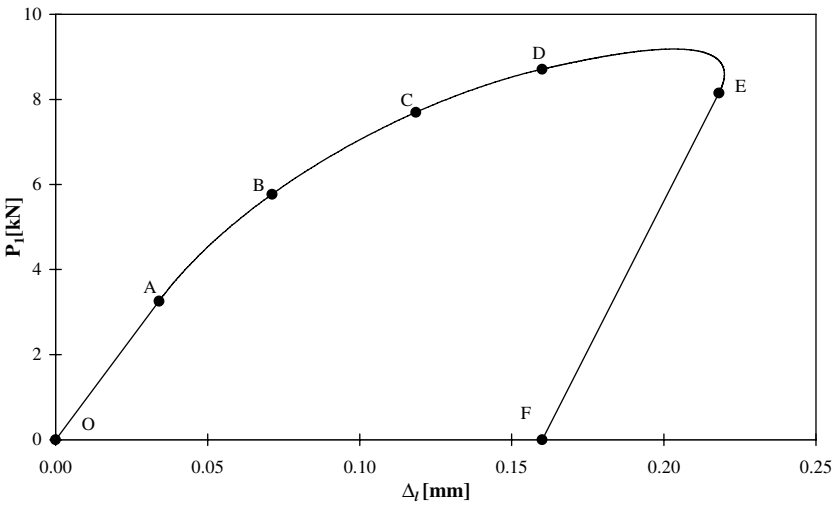

Fig. 10. Full-range load–displacement curve ($L = 25$ mm).

debonded length at the right d continues to increase until the right peak shear stress τ_f reaches $x = 0$ (Fig. 5j and point E in Fig. 7), hereby the interface enters the softening–debonding state. Thereafter, the displacement reduces linearly with the load (Fig. 5k and EF in Fig. 7) until the joint completely fails (point F in Fig. 7).

It may be noted that debonding always initiate at the right end. Even when P_2 is very close to P_1 (i.e. β approaches 1), debonding does not occur at the left end until the debonding that initiates at the right end reaches the left end (i.e. attainment of complete debonding of the plate from the concrete). Fig. 8 shows the interfacial shear stress distributions (thus the propagation of debonding) at various stages for the reference case with $\beta = 0.99$. Softening starts at almost the same time at both ends: at $P_1 = 2.544$ kN at the right compared with at $P_1 = 2.567$ kN at the left (Fig. 8a). When $P_1 = 6.59$ kN, the softening zone at the left reaches the maximum length and 40 mm of the plate at the right has debonded. The loads increase quickly

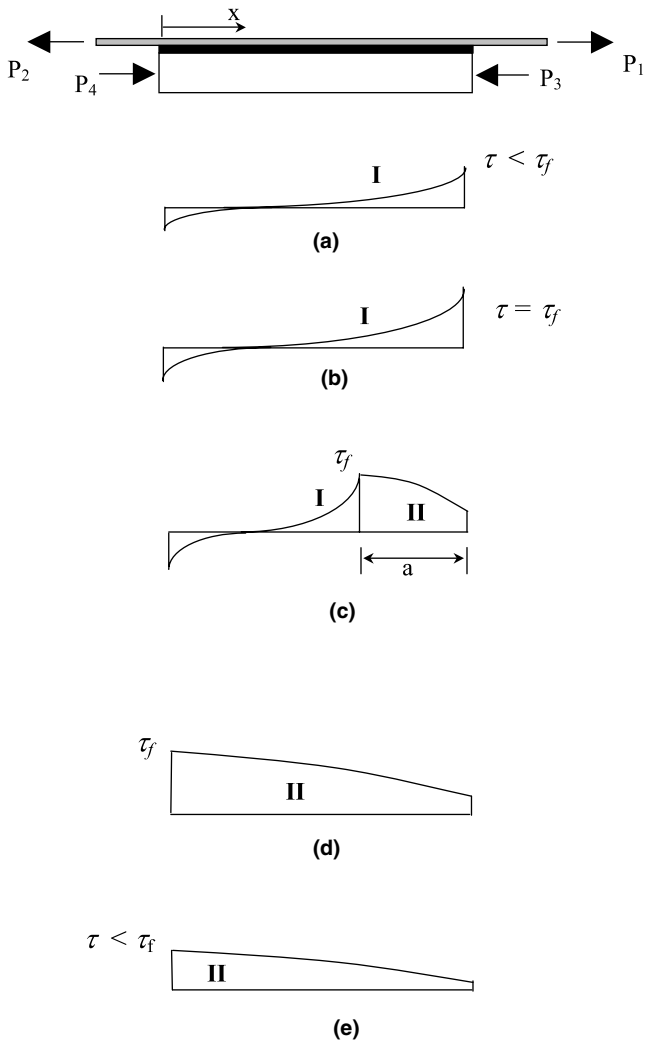

Fig. 11. Interfacial shear stress distributions at various stages ($L = 10$ mm $< a_u = 17.5$ mm). (a) Elastic stress state (OA in Fig. 12). (b) Initiation of softening at $x = L$ (point A in Fig. 12). (c) Propagation of softening zone (AB in Fig. 12). (d) Peak shear stress at $x = 0$ (point B in Fig. 12). (e) Linear unloading (BC in Fig. 12).

thereafter as the debonding on the right continues to propagate but the length of the softening zone on the left decreases (Fig. 8a). When P_1 increases to 36.19 kN, the left side is reversed to an elastic state. The maximum load of $P_1 = 38.95$ kN is reached shortly after that (Fig. 8b). When P_1 reduces to 34.66 kN, the left end enters a softening state again but the shear stresses are now opposite in direction to those of the first softening state. Thereafter, the interfacial shear stresses reduce linearly with the loads until the complete debonding of the plate.

6.3. Failure process 3 ($0 \ll \beta < 1$ and L close to a_u)

The parameters of this example are the same as those of the reference case except that the bond length L is reduced from 100 to 25 mm. Fig. 9 shows the interfacial shear stress distributions and propagation of debonding at various stages. The calculated full-range load–displacement curve is shown in Fig. 10. At early loading stages, the interface experiences progressively E (Fig. 9a and OA in Fig. 10), E–S (Fig. 9c and AB in Fig. 10), S–E–S (Fig. 9e and BC in Fig. 10) states. This process is the same as that of the preceding example.

When L is close to a_u as in this example, debonding does not occur before the left softening zone experiences unloading and its length e reduces to 0 (Fig. 9f and point C in Fig. 10). The interface returns to an E–S state (Fig. 9g and CD in Fig. 10). Debonding initiates at $x = L$ when τ decreases to 0 there (Fig. 9h and point D in Fig. 10). Thereafter, the interface enters an E–S–D state as debonding propagates and the peak shear stress τ_f moves towards the left. The maximum load P_1 is attained at this stage and then unloading occurs until complete debonding is reached, in the same manner as the preceding example (Fig. 9i-k and DE in Fig. 10 vs Fig. 5i–k and DE in Fig. 7). Clearly, shortening the bond length L from 100 mm in the previous example to 25 mm here significantly reduces the length of segment CD in the load–displacement curve, without significantly affecting the ultimate load (Fig. 7 and 10).

6.4. Failure process 4 ($L < a_u$)

In this example, the bond length is further reduced to $L = 10$ mm which is less than the characteristic softening length $a_u = 17.5$ mm. The results are shown in Figs. 11 and 12. As in the previous two examples,

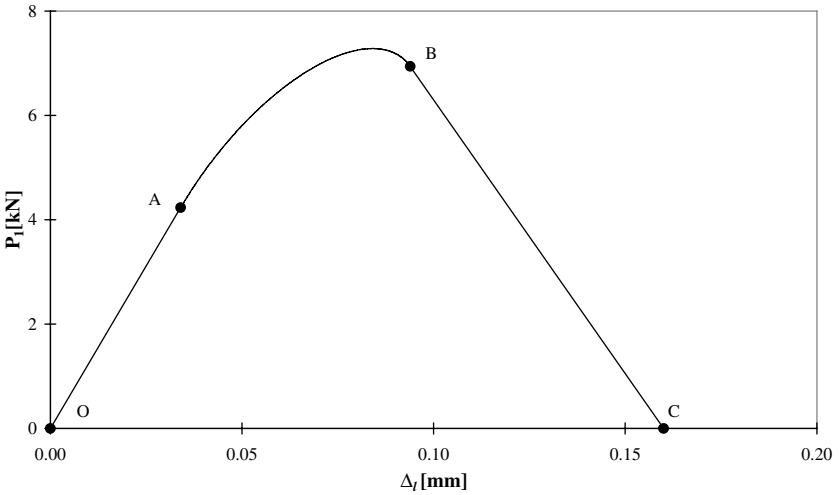

Fig. 12. Full-range load–displacement curve ($L = 10$ mm).

the interface experiences the E and E–S states (Fig. 11a–c and segment OAB in Fig. 12) at the early loading stages. However, the ultimate load P_1 is attained at the E–S stage in this example (Fig. 11c and AB in Fig. 12). As the length of the softening zone a continues to increase, the whole interface becomes a single softening zone before the right end reaches debonding (Fig. 11d and point B in Fig. 12). After this, the displacement reduces linearly with the load (Fig. 10e and BC in Fig. 12) until the joint completely fails (point C in Fig. 12). There are two major differences between this example and the two previous examples, as a result of the short bond length of 10 mm: (a) there is no softening zone starting from the left end ($x = 0$) and no debonding (macro-cracking) occurs until the complete failure of the interface; (b) the displacement increases linearly as the load decreases in the final unloading branch, whilst the displacement decreases with loading in the two preceding examples.

6.5. Failure process 5 ($\beta = 1$)

A special case with the loads acting on both ends of the FRP being equal, i.e. $P_1 = P_2$ ($\beta = 1$), is discussed here. Fig. 13 shows the interfacial shear stress distributions and propagation of debonding for $L = 10$, 25 and 100 mm. It should be noted that for all three different bond lengths, the interface

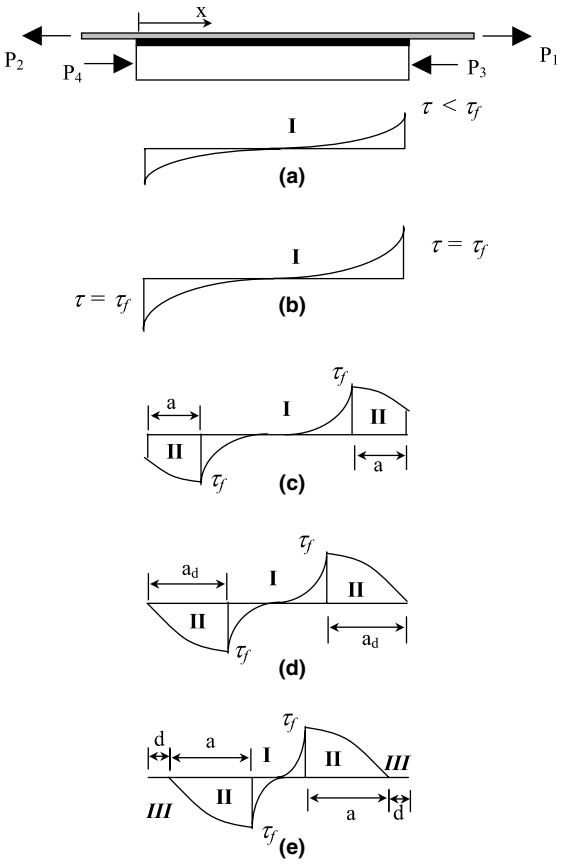

Fig. 13. Interfacial shear stress distributions at various stages ($\beta = 1$). (a) Elastic stress state (OA in Fig. 14). (b) Initiation of softening at $x = 0$ and $x = L$ (point A in Fig. 14). (c) Propagation of softening zone at $x = 0$ and $x = L$ (AB in Fig. 14). (d) Initiation of debonding at $x = 0$ and $x = L$ (point B in Fig. 14). (e) Propagation of debonding (after B in Fig. 14).

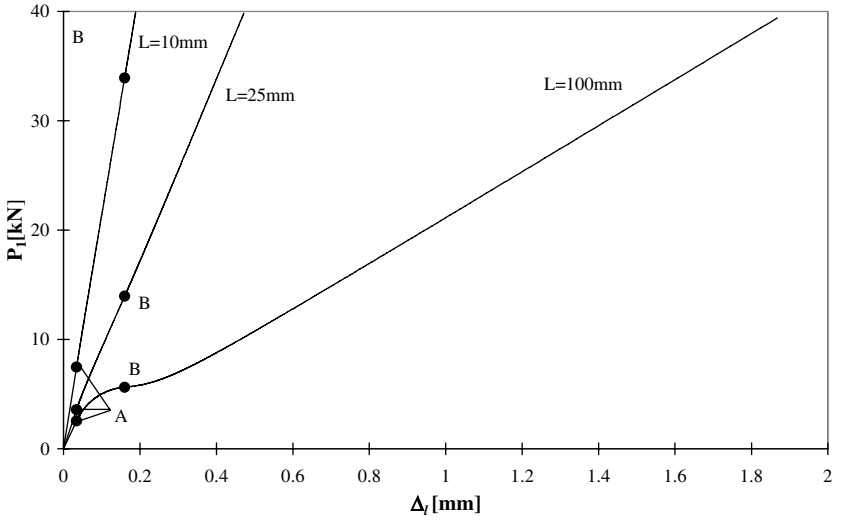

Fig. 14. Load–displacement curves ($\beta = 1$).

experiences the same sequence of interfacial shear stress distribution. The corresponding load–displacement curves are shown in Fig. 14, which however are very different in shape. Because both the geometry and the loading are symmetrical, the interfacial shear stress distribution is anti-symmetrical about $x = L/2$ in this case. The interface enters an S–E–S state (Fig. 13c and AB in Fig. 14) after τ reaches τ_f simultaneously at both the left and right ends (Fig. 13b and point A in Fig. 14). Debonding initiates when τ decreases to 0 at both ends (Fig. 13d and point B in Fig. 14) and then propagates from both ends towards the middle of the interface that is now in a D–S–E–S–D state. As both peak shear stresses τ_f continue to move towards $x = L/2$ from both sides, the load continues to increase. The ultimate load becomes infinite if material failure of the plate is not considered. It should be noted that these predictions by an idealized model for an extreme case should be interpreted with some realism in mind, as for this extreme case, the results may be rather sensitive to certain idealisations such as the exclusion of bending stresses in the plate. In addition, the stresses in the plate at two adjacent cracks in an RC beam are always different, however small this difference may be. Therefore, an infinite ultimate load could not be achieved in practice even if the material would be infinitely strong. Nevertheless, this prediction does illustrate the significance of the interaction between the two forces acting at the both ends of the plate.

7. Ultimate load

The effects of several key factors on the ultimate load $P_{1,u}$ are investigated here. Fig. 15 shows the relationship between the ultimate load and the bond length L for different β values. For a given β value, $P_{1,u}$ increases with L but remains constant after L reaches a certain value. Therefore, there exists an effective bond length beyond which an extension of the bond length cannot increase the ultimate load, as in a simple pull test of FRP-to-concrete bonded joints ($\beta = 0$, Chen and Teng, 2001). The same figure is alternatively shown in Fig. 16, where the bond length is normalised against the characteristic softening length a_u. It is seen that the normalised effective length is about 1.2 for all curves except for the one with $\beta = 0$ which has a larger value (about 1.6). Therefore, $L_e \approx 1.2a_u$ represents a good estimate for the effective

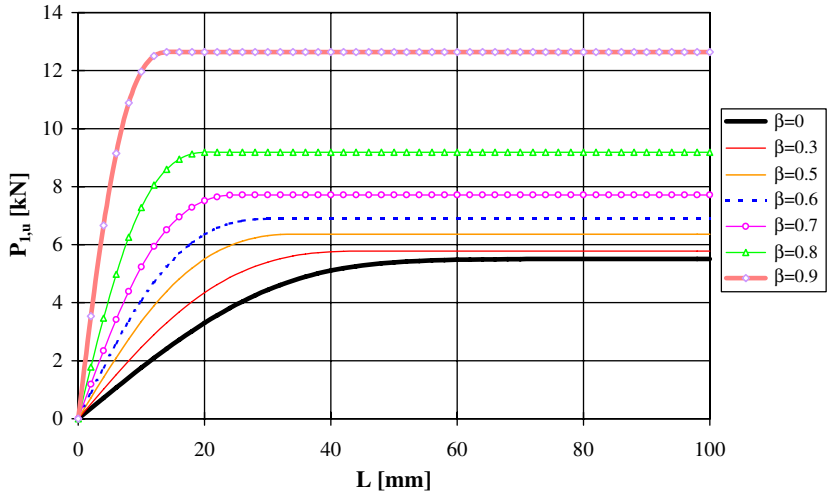

Fig. 15. Relationship between ultimate load and bond length for different β.

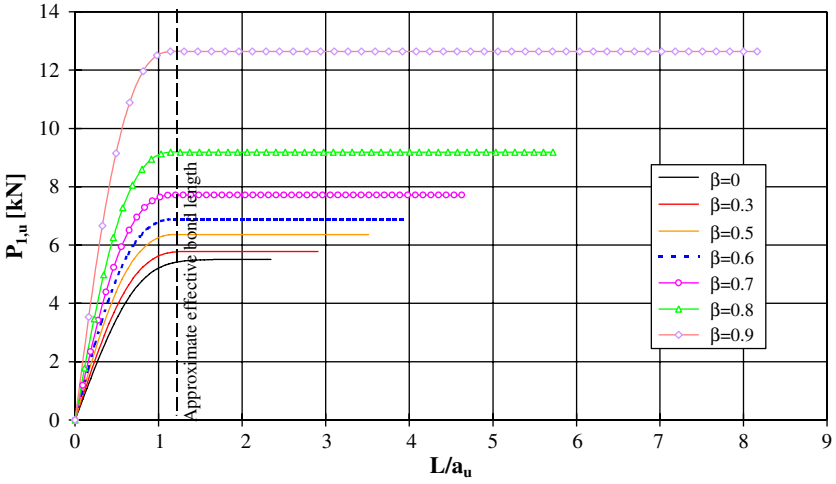

Fig. 16. Ultimate load versus normalised bond length for different β.

bond length for all cases unless β is close to zero. Even for the latter case, the ultimate load with a bond length equal to this effective bond length is very close to the ultimate load with a much longer bond length.

For the considered range of values as shown in Fig. 17a, the load parameter η is found to have little (less than 0.1%) effect on the ultimate load. An investigation into the effect of η on the ultimate load over a much larger range reveals that the ultimate load varies slowly but almost linearly with η. When η increases from 0 to 100 (corresponding to a uniform compressive stress of 37.6 MPa in the concrete prism), the ultimate load is reduced by only 9.7% (Fig. 17b). It may be argued that the concrete adjacent to the FRP is in tension in a real beam. For FRP strengthened concrete tensile members, the concrete is

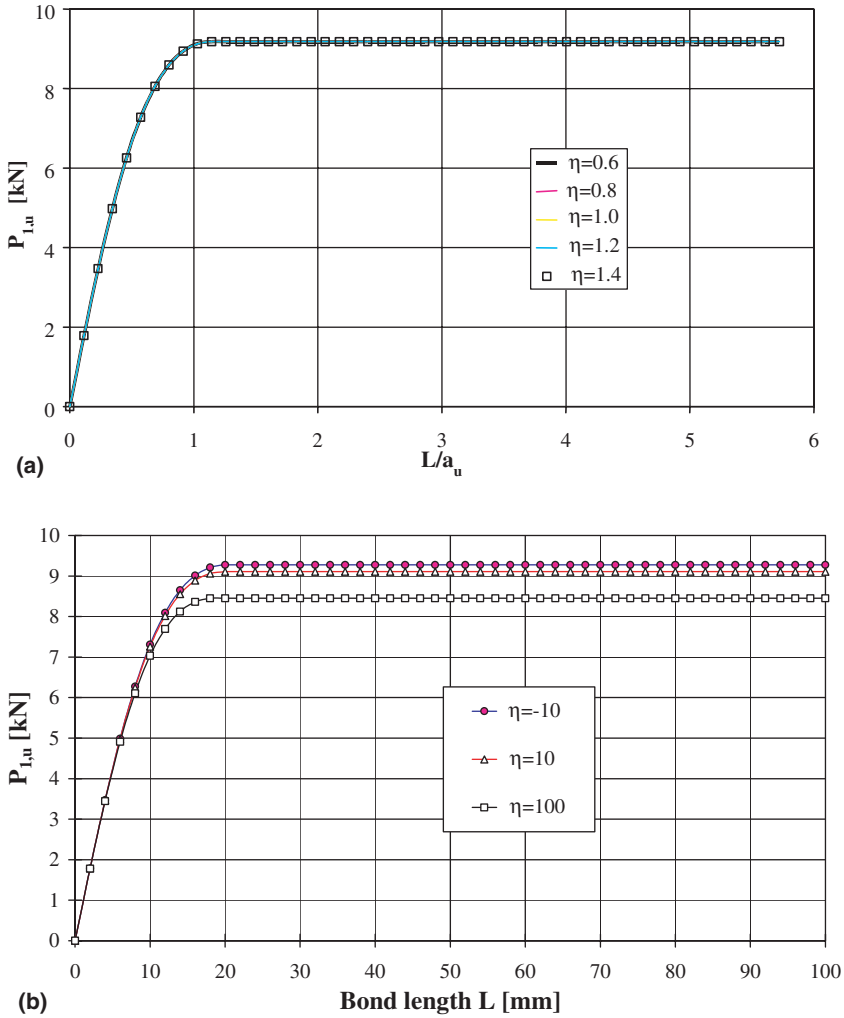

Fig. 17. Ultimate load versus bond length for different η. (a) Small range of η value and (b) large range of η value.

clearly in tension. The effect of the tensile deformation in concrete may be investigated by imposing tensile P_3 and P_4 (i.e. negative η values). When η decreases from 0 to -10 (corresponding to a uniform tensile stress of 4.1 MPa in concrete at ultimate load) in this example, the ultimate load increases by less than 1%. Since this is close to the upper limit of tensile strength of normal concrete, it may be concluded that the concrete tensile deformation is small and beneficial and may therefore be conservatively ignored.

The effect of β on the ultimate load is more clearly shown in Fig. 18. The ultimate load increases with β and the increase is more significant when the bond length is small. This increase is smooth and slow when β is small, but becomes dramatic when β approaches to 1. The ultimate load becomes infinite for any L when $\beta = 1$. It may be noted that theoretically, $\beta = 1$ in a pure bending zone in an RC beam. This may explain why intermediate crack induced debonding (Teng et al., 2003b) in soffit plated RC beams normally does not initiate within the pure bending zone but at the end of this zone where the plate stress starts to experience more rapid variations.

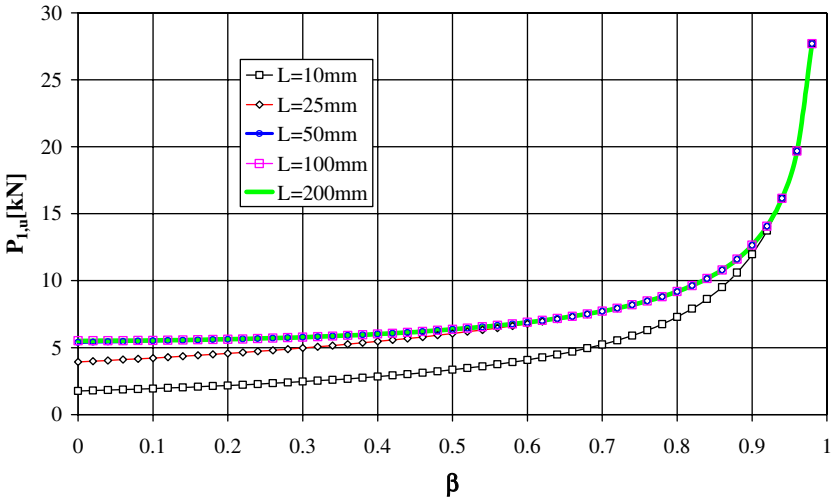

Fig. 18. Ultimate load versus β for different bond lengths.

8. Characteristic softening length a_u

It is demonstrated that the characteristic softening length a_u is an important parameter affecting the bond behaviour and the ultimate load. It is clear from Eqs. (64) and (29) that it depends on the local bond-slip properties τ_f, δ_1 and δ_f, the load parameters β and η, the plate stiffness $E_p t_p$, the concrete stiffness $E_c t_c$, and the plate to concrete width ratio b_p/b_c. Among these, β and $E_p t_p$ play the key roles. Fig. 19 shows that a_u reduces as β increases for the reference case. This reduction is almost linear for $\beta < 0.6$. It decreases

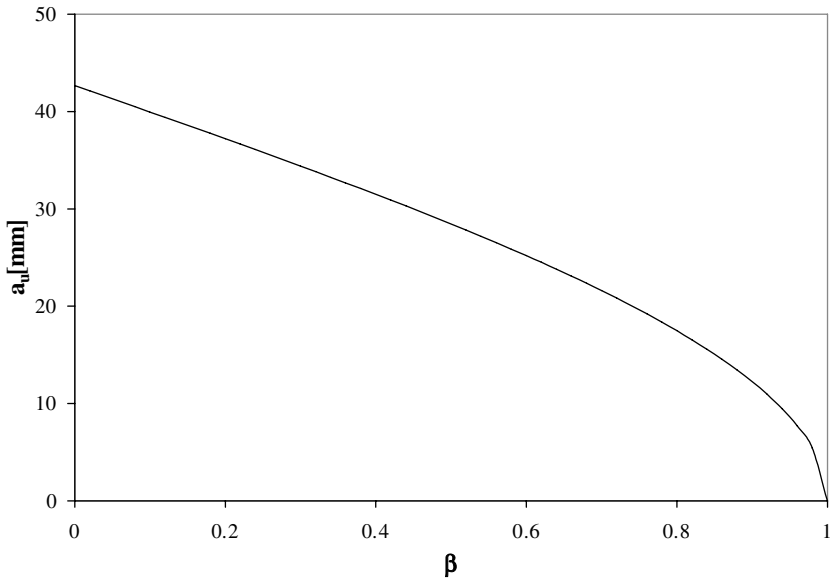

Fig. 19. Effect of load parameter β on softening length a_u.

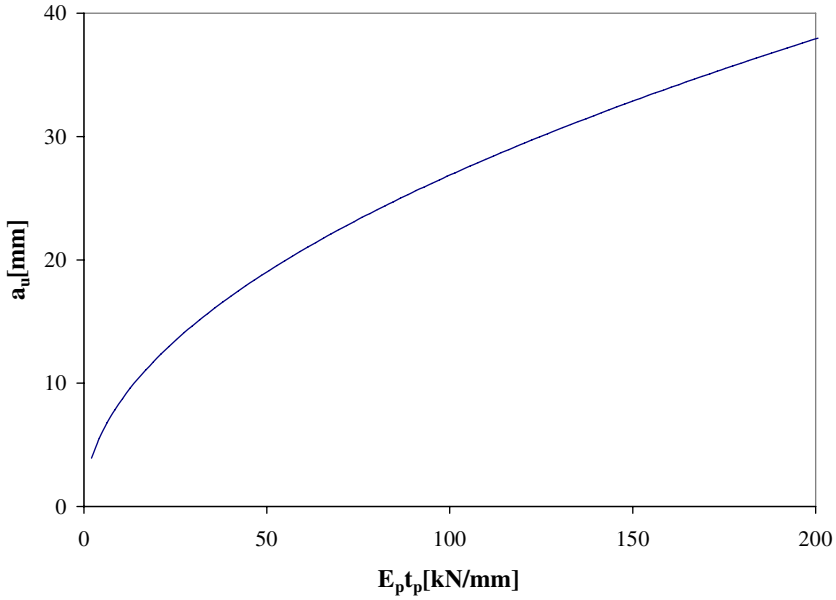

Fig. 20. Effect of plate stiffness on softening length a_u.

more quickly for large β values and reduces to 0 when $\beta = 1$ at which the ultimate load becomes infinite. Fig. 20 shows that a_u increases nonlinearly with increases of plate stiffness $E_p t_p$.

9. Conclusions

This paper has employed a simple model to investigate the behaviour of the FRP-to-concrete interface between two adjacent cracks in flexurally strengthened RC beams. An analytical solution has been presented to predict the entire debonding process of the model under various load combinations. The realistic bi-linear local bond-slip model is employed in the solution. The solution provides closed-form expressions for the interfacial shear stress distribution and the load–displacement response at different loading stages, providing a rigorous and complete theoretical basis for understanding the full-range load–displacement behaviour of the model. It should be noted that while the emphasis of the paper is on FRP-to-concrete bond interfaces, the analytical solution is equally applicable to similar interfaces between thin plates of other materials (e.g. steel and aluminium) and concrete. It may even be applicable to thin plates bonded to members of other materials such as steel and masonry provided a bi-linear local bond-slip model remains a good approximation of the local bond behaviour. The general formulation and the solution process can also be extended to interfaces with other local bond-slip models.

The analytical solution has identified five possible failure processes for FRP-to-concrete interfaces. The bond length and the load parameter β are the key factors governing these failure processes. Each of these failure processes has been examined in detail through a numerical example. The ultimate load increases with the load parameter β and becomes infinite for any bond length if β is equal to 1 (i.e. when the FRP plate is subject to equal but opposite tensile forces at both ends). Similar to the simple pull tests of FRP-to-concrete bonded joints, an effective bond length also exists for FRP-to-concrete joints with the FRP plate tensioned at both ends. The numerical examples show that the effective bond length is about 1.2 times the characteristic softening length a_u which depends on many geometrical, material and loading

parameters. The ultimate load of the bonded joint increases with the bond length before the effective length is reached and remains constant thereafter.

Acknowledgements

The authors gratefully acknowledge the financial support provided by the Research Grants Council of the Hong Kong Special Administrative Region, China (Project No.: PolyU 5151/03E) and the Guangdong Natural Science Foundation (No. 032488).

References

Chen, J.F., Teng, J.G., 2001. Anchorage strength models for FRP and steel plates bonded to concrete. Journal of Structural Engineering, ASCE 127 (1), 784–791.

Chen, J.F., Teng, J.G., 2003. Shear capacity of FRP-strengthened RC beams: FRP debonding. Construction and Building Materials 17 (1), 27–41.

Chen, J.F., Yang, Z.J., Holt, G.D., 2001. FRP or steel plate-to-concrete bonded joints: effect of test methods on experimental bond strength. Steel and Composite Structures 1 (2), 231–244.

Hollaway, L.C., Leeming, M.B., 1999. Strengthening of Reinforced Concrete Structures Using Externally-Bonded FRP Composites in Structural and Civil Engineering. Woodhead Publishing Limited, Cambridge.

Leung, C.K.Y., 2001. Delamination failure in concrete beams retrofitted with a bonded plate. Journal of Materials in Civil Engineering, ASCE 13 (2), 106–113.

Oehlers, D.J., 1992. Reinforced concrete beams with plates glued to their soffits. Journal of Structural Engineering, ASCE 118 (8), 2023–2038.

Oehlers, D.J., 2001. Development of design rules for retrofitting by adhesive bonding or bolting either FRP or steel plates to RC beams or slabs in bridges and buildings. Composites Part A: Applied Science and Manufacturing 32, 1345–1355.

Pesic, N., Pilakoutas, K., 2003. Concrete beams with externally bonded flexural FRP-reinforcement: analytical investigation of debonding failure. Composites Part B: Engineering 34, 327–338.

Piyasena, R., Loo, Y.C., Fragomeni, S., 2004. Factors influencing spacing and width of cracks in reinforced concrete: new prediction formulae. Advances in Structural Engineering 7 (1), 49–60.

Roberts, T.M., 1989. Approximate analysis of shear and normal stress concentrations in the adhesive layer of plated RC beams. The Structural Engineer 76 (12), 229–233.

Sebastian, W.M., 2001. Significance of mid-span debonding failure in FRP-plated RC beams. Journal of Structural Engineering, ASCE 127 (7), 792–798.

Shen, H.S., Teng, J.G., Yang, J., 2001. Interfacial stresses in beams and slabs bonded with a thin plate. Journal of Engineering Mechanics, ASCE 127 (4), 399–406.

Smith, S.T., Teng, J.G., 2001. Interfacial stresses in plated beams. Engineering Structures 23 (7), 857–871.

Smith, S.T., Teng, J.G., 2002a. FRP-strengthened RC beams—I: Review of debonding strength models. Engineering Structures 24 (4), 385–395.

Smith, S.T., Teng, J.G., 2002b. FRP-strengthened RC beams—II: Assessment of debonding strength models. Engineering Structures 24 (4), 397–417.

Smith, S.T., Teng, J.G., 2003. Shear-bending interaction in debonding failures of FRP-plated RC beams. Advances in Structural Engineering 6 (3), 183–199.

Teng, J.G., Chen, J.F., Smith, S.T., Lam, L., 2002a. FRP Strengthened RC Structures. John Wiley and Sons, UK.

Teng, J.G., Zhang, J.W., Smith, S.T., 2002b. Interfacial stresses in reinforced concrete beams bonded with a soffit plate: a finite element study. Construction and Building Materials 16 (1), 1–14.

Teng, J.G., Chen, J.F., Smith, S.T., Lam, L., 2003a. Behaviour and strength of FRP-strengthened RC structures: a state-of-the-art review. Proceedings of the Institution of Civil Engineers–Structures and Buildings 156 (1), 51–62.

Teng, J.G., Smith, S.T., Yao, J., Chen, J.F., 2003b. Intermediate crack-induced debonding in RC beams and slabs. Construction and Building Materials 17 (6–7), 447–462.

Wu, Z.S., Yuan, H., Niu, H., 2002. Stress transfer and fracture propagation in different kinds of adhesive joints. Journal of Engineering Mechanics, ASCE 128 (5), 562–573.

Yang, Z.J., Chen, J.F., Proverbs, D., 2003. Finite element modelling of concrete cover separation failure in FRP plated RC beams. Construction and Building Materials 17 (1), 3–13.

Yao, J., Teng, J.G., Lam, L., 2005a. Experimental study on intermediate crack debonding in FRP-strengthened RC flexural members. Advances in Structural Engineering 8 (4), 365–396.

Yao, J., Teng, J.G., Chen, J.F., 2005b. Experimental study on FRP-to-concrete bonded joints. Composites Part B: Engineering 36 (2), 99–113.

Yuan, H., Teng, J.G., Seracino, R., Wu, Z.S., Yao, J., 2004. Full-range behavior of FRP-to-concrete bonded joints. Engineering Structures 26 (5), 553–565.